

On The Evaluation of Collision Probability along a Path

Lorenzo Paiola^{1,2}, Giorgio Grioli^{1,2}, Antonio Bicchi^{1,2}

Abstract—Characterizing the risk of operations is a fundamental requirement in robotics, and a crucial ingredient of safe planning. The problem is multifaceted, with multiple definitions arising in the vast recent literature fitting different application scenarios and leading to different computational approaches. A basic element shared by most frameworks is the definition and evaluation of the probability of collision for a mobile object in an environment with obstacles. We observe that, even in basic cases, different interpretations are possible.

This paper proposes an index we call “Risk Density”, which offers a theoretical link between conceptually distant assumptions about the interplay of single collision events along a continuous path.

We show how this index can be used to approximate the collision probability in the case where the robot evolves along a nominal continuous curve from random initial conditions. Indeed, under this hypothesis the proposed approximation outperforms some well-established methods either in accuracy or computational cost.

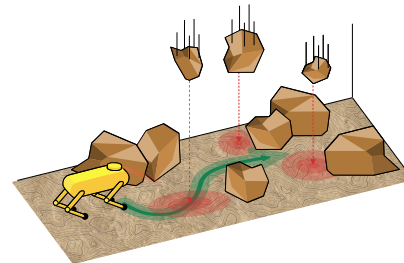
Index Terms—risk, collision, robotics, safety, probability

I. INTRODUCTION

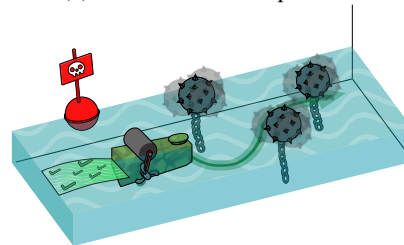
AS more and more autonomous systems are asked to perform safety-critical tasks, the importance of evaluating the *risk* associated with a set of actions of a robot is becoming paramount. Several applications, including warehouse management, autonomous driving, medical and cooperative robotics, require the system not only to be *safe* at any instant in time, but to plan actions that assure safety also in the future [1]. Uncertainty plays a central role in the process of associating a measure of how problematic planned actions could be. Indeed, what the agent knows about itself and its environment drastically affects the potential risk of its plan.

A centerpiece of risk evaluation for mobile robots is the ability to give an accurate estimate of “the probability of the robot not being able to finish the path” [2]. Indeed, this definition requires, even in the simplest case, the knowledge of the probability of collision of the robot, be it in the continuous or the discrete case [3], [4].

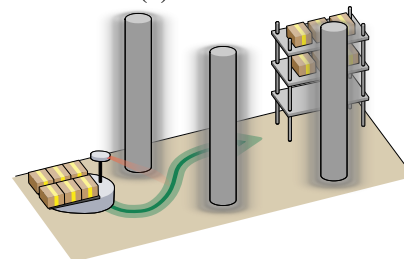
This estimation problem is still not considered solved, as all the methods found in literature, to the best of the authors’ knowledge, fail to give a good estimate of this quantity while capturing all the aspects of the problem at hand. Specifically, approximation schemes fail to assess the true value of the probability or are computationally prohibitive and usually depend on parameters foreign to the problem setting. Moreover,



(a) Hazardous mine operation.



(b) Mined sea.



(c) Unmapped warehouse.

Figure 1: Depiction of different scenarios where collisions have to be modeled in different ways. (a) shows an environment with areas where falling rocky debris could hit the robot at any point in time. (b) shows a robot boat navigating in a randomly mined body of water. (c) shows a warehouse robot navigating an uncertain environment.

even the very definition of the probability of a continuous set of events (in our case, the collision probability along a path) is not univocally defined without further assumptions about the process and the interaction between events happening at different configurations, as shown in Figure 1.

The literature reports multiple methods to evaluate event probabilities, each with merits and limitations. Monte Carlo simulations [5]–[7] can accurately estimate collision probability, but are computationally intensive since estimating the desired distribution requires a large number of samples. Moreover, the discrete and “batch” nature of Monte Carlo methods is at odds with a continuous optimization framework [8]. Approaches to lower the computational hardness of this method are possible:

¹Soft Robotics for Human Cooperation and Rehabilitation, Istituto Italiano di Tecnologia, Genova 16163, Italy (lorenzo.paiola@iit.it).

²Department of Information Engineering and Centro di Ricerca “Enrico Piaggio”, University of Pisa, 56122, Pisa, Italy.

e.g., [9] uses importance sampling techniques to make the simulations satisfy real-time requirements.

Chance constraints (CC) [4], [10]–[12] indicate imposed restrictions on the states which have to hold in a probabilistic sense. CCs can concern either single events or, more commonly, joint sets of these. Joint chance constraints (JCC) [13] then require an evaluation of the probability of the set of events which, in our case, is the set of collision events along a path. Unfortunately, JCC generally have to be approximated to be used, as their interdependent nature makes them hard to evaluate either computationally or analytically.

JCC evaluation can be computed either at once, or sequentially. In both cases, several techniques have been developed to tackle this evaluation. In the first category, we find Ellipsoidal approximations [13] that simplify the multivariate integral of the joint constraint to be one-dimensional, offering good computational performance, but approximating the actual value in a very conservative way. Instead of evaluating the joint constraint at once, sequential methods consist in subdividing the JCC into individual CCs and combining their appraised value. Indeed, in this case, the approximation to be employed is two-fold: both the value of each singular CC and their mutual interaction are simplified for computation. In practice, either Boole’s Lemma is used to relax the joint constraint into a sum of multiple simpler scalar chance constraints [14], or the constraints are considered independent variables and combined in a multiplicative way. Individual chance constraints can be translated to deterministic ones using the approximations used for joint constraints or by using more ad-hoc approaches [10], [15]–[17]. The additive relaxation result of Boole’s Lemma is known to be conservative. However, techniques such as risk-allocation [3], [18] can mitigate this by assigning a larger “probability mass” to stages of the path where the collision is more likely.

Occupancy grids methods [2], [19], [20] are another prevalent choice used for obstacle avoidance. Such approaches discretize the robot workspace in cells and assign an occupancy probability value to each cell to perform risk evaluation. Grid-based methods, by considering each cell of the grid independent from one another, use a multiplicative relaxation of the cumulative probability. While being the most popular choice to compute the collision probability along a path, grid-based approaches are limited. Indeed, choosing a discretization mesh severely influences the computed value of the collision probability [21].

All the previous approaches, except for Monte Carlo sampling, work well for linear problems and Gaussian random variables. More general approaches exist, able to tackle both nonlinear systems and more general random variables via Lasserre Hierarchy [22], [4], but these are computationally prohibitive. The language of exit times is used in [8] to derive an estimate in a continuous and nonlinear setting, but considers only the robot uncertainty.

A. Contribution

Our contribution is to illustrate some of the problems encountered in applying Grid-Based and JCCs methods and to propose a novel method to characterize and approximate

the robot collision probability along a continuous trajectory. To do so, we focus on a well-defined case with deterministic dynamics, where a rigorous definition of the collision probability along a continuous path can be given. The proposed approximation shows better or comparable accuracy to other approaches while being computationally competitive. This approximation depends on the objects’ combined dimension and a quantity, which we call risk density, that depends only on the parametrization of the path followed by the robot, the obstacle position, and no exogenous parameters. Additionally, this metric gauges the continuous path as a whole instead of subdividing it into waypoints. We stress that our intent is both to highlight the existence of the problem and to give computationally tractable tools to tackle it.

The paper is organized as follows. Section II explores how the probability of intersection between two uncertain shapes can be formalized and computed. In Section III we discuss how this formalization translates to the problem of collision probability computation along a continuous path. In this section, we discuss some possible assumptions about the interdependence of events and define the probability of collision as a consequence; secondly, we discuss an example of how this probability can be computed and highlight some issues due to the continuity of the problem. Section IV briefly describes current approaches and their limitations. In Section V, we propose the *Risk Density* index, briefly discuss its relevance and introduce an approximation to the collision probability along a continuous path. In Section VI, we display the computational experiments we have carried out as validation and compare our approximation performance to other techniques. In Section VII we discuss the properties of the approach and how these are revealed in the benchmark proposed while also highlighting the limitations of the method. In Section VIII we show how the same *Risk Density*, can be used to correct a previously computed Monte Carlo estimate, after the simulation setting has been altered. Finally, in Section IX some applications of *Risk Density* in a trajectory optimization setting are presented. Section X concludes the paper.

II. BACKGROUND

Consider a robot and an obstacle immersed in a workspace $\mathbb{W} \subseteq \mathbb{R}^n$. Let $\mathbb{X}_R(x_R) \subseteq \mathbb{W}$ be the set of points occupied by the robot and $\mathbb{X}_O(x_O) \subseteq \mathbb{W}$ the set occupied by the obstacle, where $x_R, x_O \in \mathbb{W}$ are the reference frames locations for the robot and obstacle, respectively.

The overlap condition [10], [23] defined as

$$C^{[0]}(x_R, x_O) : \mathbb{X}_R(x_R) \cap \mathbb{X}_O(x_O) \neq \emptyset, \quad (1)$$

indicates wherever the two sets of points intersect, or in other words, that a collision has happened if we consider a dynamic scenario.

The GJK algorithm [24] is a standard practical tool to check eq. (1) when all the information about the shape and position of both the robot and object is wholly known. One of its building blocks is the notion of Minkowski sum on sets,

$$A \oplus B := \{a + b | a \in A, b \in B\}, \quad (2)$$

which can be used to define an equivalent condition to eq. (1), which is

$$C^{[0]}(x_R, x_O) : \{\bar{0}_n\} \subseteq \mathbb{X}_R(x_R) \ominus \mathbb{X}_O(x_O), \quad (3)$$

where $\bar{0}_n \in \mathbb{R}^n$ is the n -dimensional origin and $A \ominus B \triangleq A \oplus (-B)$ is sometimes known as Minkowski difference.

Unfortunately, the GJK algorithm is rendered useless as soon as uncertainty is introduced in the problem. In fact, even assuming that both the obstacle and the robot are perfectly known in shape but uncertain in position, condition eq. (1) cannot be checked in a deterministic way anymore, and we are required to define and appraise an overlap/collision probability.

A possible way to define such a probability is to resort to an *indicator function*, defined from (1) as

$$I_{C^{[0]}}(x_R, x_O) = \begin{cases} 1 & \text{if } \mathbb{X}_R(x_R) \cap \mathbb{X}_O(x_O) \neq \{\emptyset\}, \\ 0 & \text{otherwise.} \end{cases} \quad (4)$$

Now, if we consider x_R and x_O to be realizations of two random variables, R and O , characterized by a joint probability density function $f_{R,O}(r, o)$, the overlap or collision probability is

$$P(C^{[0]}) = \int_{\mathbb{W}} \int_{\mathbb{W}} I_{C^{[0]}}(r, o) f_{R,O}(r, o) dr do. \quad (5)$$

While (5) gives the actual value of $P(C^{[0]})$, its numerical computation is, in general, not trivial as it consists of two multidimensional integrals in \mathbb{R}^n , where at each point (r, o) one should calculate $I_{C^{[0]}}$, e.g. via GJK. However, that analysis can be simplified by resorting to (3) and shifting to another perspective. In a similar fashion to [15], we decompose the uncertain sets \mathbb{X}_R and \mathbb{X}_O as

$$\mathbb{X}_R = S_R + d_R + N_R(\omega), \quad (6)$$

$$\mathbb{X}_O = S_O + d_O + N_O(\omega), \quad (7)$$

as shown in Figure 2. Now $S_R \subseteq \mathbb{W}$ and $S_O \subseteq \mathbb{W}$ are sets centered in the origin of the deterministic shapes, $d_R, d_O \in \mathbb{W}$ are vectors equal to the mean of R and O respectively, while N_R and N_O are zero-mean Random Variables such that $R = d_R + N_R$, $O = d_O + N_O$.

Condition (3) becomes equivalent to

$$\{0\} \subseteq \mathbb{X}_R(R) \ominus \mathbb{X}_O(O)$$

$$\iff \{0\} \subseteq (S_R \ominus S_O) + (d_R - d_O) + (N_R - N_O)$$

$$\iff \{0\} \subseteq S_{RO} + d_{RO} + N_{RO}$$

$$\iff N_{OR} \in S_{RO} + d_{RO} \quad (8)$$

$$\iff d_{OR} + N_{OR} \in S_{RO}, \quad (9)$$

where

$$d_{RO} = d_R - d_O = -d_{OR}, \quad (10)$$

is the distance vector between the mean of the two random variables and

$$N_{RO} = N_R - N_O = -N_{OR}, \quad (11)$$

is a zero-mean Random Variable describing the uncertainty of such a vector.

Using conditions (8) and (9), both derived from the set decomposition, (5) can be restated in as either

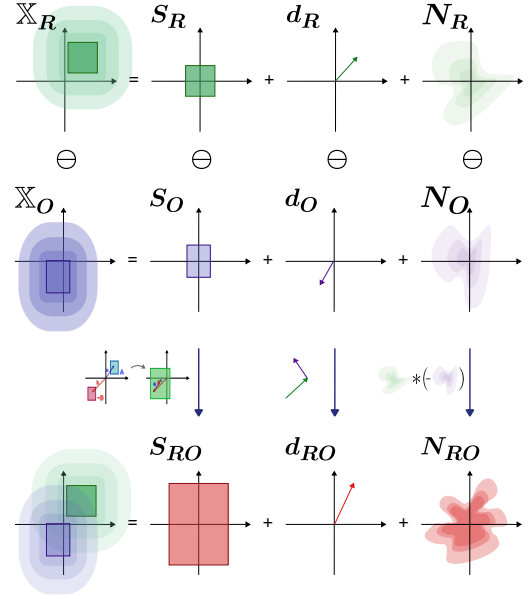


Figure 2: Graphical depiction of the decomposition of the robot and obstacle sets. The result of the Minkowski sum is also illustrated. Each object is represented by its shape, the vector pointing to its frame of reference, and a Random Variable describing the uncertainty in its position.

$$\begin{aligned} P(C^{[0]}) &= \int_{S_{RO}} (f_{N_{OR}}(x) * \delta_{d_{OR}}(x)) dx \\ &= \int_{S_{RO}} f_{N_{OR}}(x + d_{OR}) dx \end{aligned} \quad (12)$$

or

$$P(C^{[0]}) = \int_{S_{RO} + d_{RO}} f_{N_{OR}}(x) dx. \quad (13)$$

Here $f_{N_{OR}} = f_{N_O} * f_{N_{-R}}$ is the probability density function resulting from the difference $N_O - N_R$, while $\delta_{d_{OR}}(x)$ is the Dirac delta function centered in d_{OR} . Both eq. (12) and eq. (13) are computed via a single integral on a defined set in contrast to eq. (5). All the remaining complexity hides inside $f_{N_{OR}}$ since, in general, computing this pdf requires a convolution operation.

This may not be an issue in the case when the convolution has closed form expression, e.g. if R and O are normally distributed as $R \sim \mathcal{N}(\mu_R, \Sigma_R)$, $O \sim \mathcal{N}(\mu_O, \Sigma_O)$. In that case eq. (12) and eq. (13) simplify [25] to

$$P(C^{[0]}) = \int_{S_{RO}} \mathcal{N}(x | \mu_O - \mu_R, \Sigma_T) dx \quad (14)$$

$$P(C^{[0]}) = \int_{S_{RO} + (\mu_R - \mu_O)} \mathcal{N}(x | 0, \Sigma_T) dx, \quad (15)$$

where $\Sigma_T = \Sigma_R + \Sigma_O$.

III. PROBLEM STATEMENT

Having formalized the probability of a collision event in a fixed configuration in Section II, we now approach the problem of defining the same quantity along a path followed by the robot. A path is a function $\mu_R(s) : \mathbb{S} \rightarrow \mathbb{W}$ going from a possibly continuous ordered set of configurations $\mathbb{S} = \{s_0, s_1, \dots, s_N\}$

to the workspace.

Denoting \mathcal{W} as a sufficiently well-behaved family of sets in \mathbb{W}^1 , i.e. $w_i \in \mathcal{W} \implies w_i \subseteq \mathbb{W}$, the integration set associated with each configuration s is given by the function $D_{RO}(s) : \mathbb{S} \rightarrow \mathbb{W}$,

$$D_{RO}(s) = S_{RO} + (\mu_R(s) - \mu_O). \quad (16)$$

We also explicitly consider the dependence on s of N_{RO} on s by treating it as a stochastic process $N_{RO}(\omega, s) : \Omega \times \mathbb{S} \rightarrow \mathbb{W}$, where Ω is the sample space. Similarly to condition eq. (8), we associate each configuration s to the stochastic process $C(\omega, s) : \Omega \times \mathbb{S} \rightarrow \{0, 1\}$,

$$C(\omega, s) : N_{RO}(\omega, s) \in D_{RO}(s), \quad (17)$$

and, with a slight abuse of notation, we parametrize the stochastic collision event as

$$\begin{aligned} C_s &:= \{\omega \in \Omega | C(\omega, s) = 1, s \in \mathbb{S}\} \\ &= \{\omega \in \Omega | N_{RO}(\omega, s) \in D_{RO}(s), s \in \mathbb{S}\}, \end{aligned} \quad (18)$$

i.e. the set of all possible outcomes which result in a collision in s . Consequently each configuration has an associated probability in the form of eq. (15) as

$$P(C_s) = \int_{D_{RO}(s)} \mathcal{N}(x|0, \Sigma_T) dx. \quad (19)$$

In general both the robot and the obstacle dynamics can be stochastic, making the random process $N_{RO}(\omega, s)$ at each s correlated to the history of past configurations. In general, to model the dynamics of such a process, the tools of Itô Calculus [26] are to be used. However in this paper we assume that the stochastic process is identically distributed, i.e. $N_{RO}(\omega, s_i) \sim \mathcal{N}(0, \Sigma_T)$.

While eq. (19) is valid for an isolated configuration s , interactions between neighboring configurations in \mathbb{S} must be accounted for if a path is considered.

Indeed what we are interested in is the value of

$$P(C) := P\left(\bigvee_{\mathbb{S}} C_s\right), \quad (20)$$

which however is not directly computable due to the non trivial dependence between events (18).

A. Assumptions

To model such interactions, and to compute eq. (20), it is necessary to specify further hypotheses which apply to different cases. An assumption that is commonly adopted is to consider that all collision events are independent (e.g. [27]). Formally, this model can be described as

(H1) $C_{s_i} \perp C_{s_j}, \forall s_i \neq s_j \in \mathbb{S}$,

leading to the following lemma.

Lemma 1 (H1). *The probability of collision eq. (20) under (H1) reduces to*

$$P_{H1}(C) = 1 - \prod_{\mathbb{S}} (1 - P(C_s)), \quad (21)$$

where $P(C_s)$ is eq. (19).

Proof.

$$\begin{aligned} P\left(\bigvee_{\mathbb{S}} C_s\right) &= P\left(\overline{\bigwedge_{\mathbb{S}} \overline{C_s}}\right) = 1 - P\left(\bigwedge_{\mathbb{S}} \overline{C_s}\right) \xrightarrow{\text{ind}} \\ &\xrightarrow{\text{ind}} 1 - \prod_{\mathbb{S}} (1 - P(C_s)), \end{aligned} \quad (22)$$

□

While this premise is reasonable in the discrete case, it is easy to show that it leads to incongruities as we approach a continuous path. As pointed out by [9], the assumption is *asymptotically tautological*, as the estimation of the collision probability resulting from (H1) converges to 1 with the cardinality of the set $|\mathbb{S}| \rightarrow \infty$. Hence with increasing the path discretization resolution, all paths would almost surely lead to collision.

To fix this issue (H1) needs to be relaxed. A less restrictive alternative to the independence hypothesis is the assumption that the collision event is Markovian: the events C_s depend only on the immediately preceding past, i.e. $P(C_{s_j} | \overline{C_{s_{j-1}}}, \dots, \overline{C_{s_0}}) = P(C_{s_j} | \overline{C_{s_{j-1}}})$. In this case the conditioned probability is analytically unapproachable in general, and approximations about its formulations are to be introduced. For instance, the authors of [28] use truncated Normal distributions to model preceding configurations being collision-free. We introduce here a different simplification: we consider that the collision could only happen on newly swept “area” in \mathbb{W} at each index s_i . More precisely we assume that

(H2)

- C_s has the Markov property
- $P(C_{s_{i+1}} | \overline{C_{s_i}}) = P(N_{RO}(s_{i+1}) \in (D_{RO}(s_{i+1}) \cap D_{RO}^C(s_i)))$, where $D_{RO}^C(s)$ denotes the complement of the set $D_{RO}(s)$.

Lemma 2 (H2). *The probability of collision eq. (20) under (H2) reduces to*

$$P_{H2}(C) = 1 - \prod_{s_i \in \mathbb{S}} (1 - P(C_{s_{i+1} \cap \overline{s_i}})), \quad (23)$$

where

$$\begin{aligned} C_{s_{i+1} \cap \overline{s_i}} &:= \\ &\{\omega \in \Omega | N_{RO}(\omega, s_{i+1}) \in (D_{RO}(s_{i+1}) \cap D_{RO}^C(s_i))\}. \end{aligned} \quad (24)$$

Proof.

$$\begin{aligned} P\left(\bigvee_{\mathbb{S}} C_s\right) &= P\left(\overline{\bigwedge_{\mathbb{S}} \overline{C_s}}\right) = 1 - P\left(\bigwedge_{\mathbb{S}} \overline{C_s}\right) \xrightarrow{\text{mark}} \\ &\xrightarrow{\text{mark}} 1 - \prod_{s_i \in \mathbb{S}} (1 - P(C_{s_{i+1}} | \overline{C_{s_i}})) \stackrel{\text{eq. (24)}}{=} \\ &\stackrel{\text{eq. (24)}}{=} 1 - \prod_{s_i \in \mathbb{S}} (1 - P(C_{s_{i+1} \cap \overline{s_i}})). \end{aligned}$$

□

An alternative model underpinning a different path integral extension of the collision probability formula stems from

¹For example the Borel algebra of \mathbb{W} , $\mathcal{B}(\mathbb{W})$.

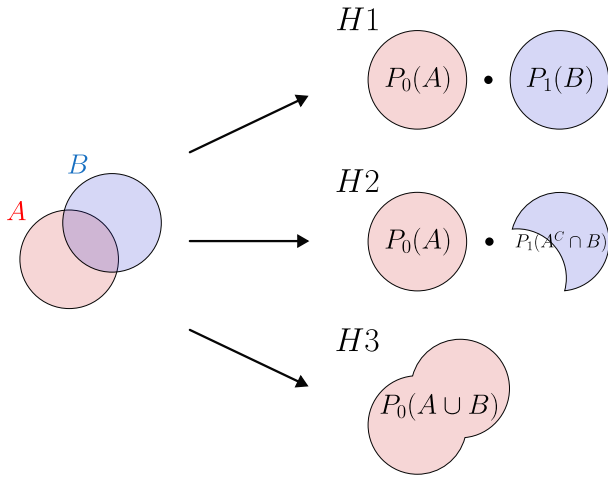


Figure 3: Visual representation of how considered assumptions work on two sub-events. The events considered are $\{\omega | N_{RO}(s_0, \omega) \in A\}$ and $\{\omega | N_{RO}(s_1, \omega) \in B\}$, where the sets A and B are shown as red and blue disks. $P_0(\cdot)$ and $P_1(\cdot)$ stand respectively for the probability measure of the first and the second random variable to be inside a set.

considering the evolution of the robot path as completely deterministic, while limiting the uncertainty to the sole knowledge of the initial obstacle and robot position. This premise can be formally stated using the concept of stopped process [29].

(H3) $N_{RO}(\omega, s)$ is a stopped process $N_{RO}^{s_0}(\omega, s) := N_{RO}(\omega, \min(s_0, s))$.

In this case the stochastic process is constant, as s_0 is the first element of \mathbb{S} , meaning that all the uncertainty can be represented as a single Random Variable $N_{RO}^{s_0}(\omega)$ sampled from a sample space Ω .

We then introduce eq. (20) under (H3):

Lemma 3 (H3). *The probability of collision eq. (20) under (H3) reduces to*

$$P_{H3}(C) = \int_{D_T} \mathcal{N}(x|0, \Sigma_T) dx, \quad (25)$$

with

$$D_T = \bigcup_{\mathbb{S}} D_{RO}(s). \quad (26)$$

Proof. $\bigvee_{\mathbb{S}} C_s = \bigvee_{\mathbb{S}} \{N_{RO}(\omega, s) \in D_{RO}(s)\} = \bigvee_{\mathbb{S}} \{N_{RO}(\omega, s_0) \in D_{RO}(s)\} = \{N_{RO}(\omega, s_0) \in \bigcup_{\mathbb{S}} D_{RO}(s)\}$, of which the probability is eq. (25). \square

Note that lemma 3 is a specialization of eq. (15) on the set D_T . Moreover, notice how by swapping D_T with the union of the $D_{RO}(s)$ over any contiguous subset of \mathbb{S} , i.e. $D_{RO}(s_1, s_2) = \bigcup_{s=s_1}^{s_2} D_{RO}(s)$, we obtain the probability of the related subpath. In this sense the ‘‘Probability To Go’’ is computed by integrating eq. (25) over $D_{RO}(s, s_N)$.

While hypotheses such as (H1), (H2) and (H3), shown in fig. 3, are mathematical abstractions, these tightly connect to the assumptions one can draw from the particular scenario. Indeed, (H1) can model fairly well an obstacle whose position changes over time with a dynamics that is much faster than that of the robot, but occupies, on average, the same regions

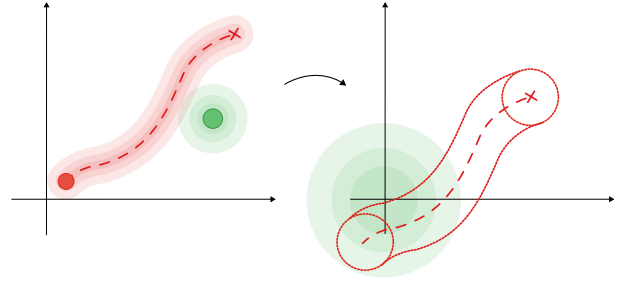


Figure 4: Interpretation of eq. (25). The problem is moved from the initial domain \mathbb{W} to the domain of the difference between the robot and the obstacle shape. This results from the transformation shown in fig. 2, which moves all the uncertainty on a single distribution centered in zero, while the integration set is D_T .

of space with a fixed frequency: think of obstacles such as a stream of people, or falling debris, or droplets of water. On the other hand (H3) would more accurately model a scenario where, for example, the obstacle is a pillar whose position is fixed but uncertain. Finally, hypothesis (H2) is the more involved assumption. This hypothesis models scenarios where collisions can occur only in the additional area covered at the last step taken. For example, consider a robot boat navigating through a minefield in the sea. It is reasonable to assume that collisions can only happen in front of the boat. However, a return trip on the same path would not be automatically safe because the mines bob with the waves and slowly change their, already uncertain, positions around their respective means. A stylized depiction of a few of these example scenarios is shown in Figure 1.

Notice that the complete set of possible scenarios form a somehow continuous spectrum in which (H1) and (H3) lie at two opposite extremes: (H1) is total independence between configurations, while (H3) denotes ‘‘total dependence’’. Multiple different modelling assumptions about the uncertainty can be found in the range in between (H1) and (H3), such as (H2). We show in simulation in Section VI how these hypotheses influence probability estimates in the same simple scenario.

B. Continuous Path Parametrization

In the case in which the set \mathbb{S} is continuous, one has either to evaluate a union of the uncountable number of sets spanned by the robot moving along the trajectory, eq. (26), or to compute the product over an uncountable number of indices. Computing the union or the product turns out to be unpractical, or even impossible in closed form. The problem is, for a path parametrized as $\mu_R(s) : [0, 1] \rightarrow \mathbb{W}$, to find an expression of $D_{RO}(s)$ and D_T eq. (26). For simplicity let us assume henceforth that $\mu_R(s)$ is almost everywhere differentiable map and $\mathbb{W} = \mathbb{R}^2$. Consider two disks S_R and S_O outer-bounding the shape of the objects. Then, the combined shape S_{RO} is a disk whose radius is the radii sum. Here D_T takes the shape of a rounded tube, drawn by the large disk being swept along the trajectory, as shown in fig. 4.

The characterization of such a swept space is generally rather complex. Recently, that characterization has been addressed by [30] with nontrivial mathematical methods, and focusing on local aspects.

Suppose a fully diffeomorphic map can parameterize the swept space

$$\Phi(s, \theta) : [0, 1] \times [-T, T] \rightarrow \mathbb{W}, \quad (27)$$

where $s \in [0, 1]$ is a line variable defined along the path $\mu_R(s)$ through which the disk is dragged, and $\theta \in [-T, T]$ is a characteristic length associated with the shape of the robot. Now, using eq. (27), eq. (25) becomes

$$P_{H3}^a(C) = \int_0^1 \int_{-T}^T \mathcal{N}(\Phi(\gamma, \nu) - \mu_O | 0, \Sigma_T) \Gamma(\gamma, \nu) d\nu d\gamma, \quad (28)$$

where $\Gamma(\gamma, \nu) = |\det(\nabla\Phi(\gamma, \nu))|$.

As explored in [31], eq. (27) can be used also to compute eq. (23) under (H2). Indeed, using the parametrization and adhering to eq. (24), the conditional probability in the continuous case can be rewritten as

$$\begin{aligned} P^a(C_{s+ds} | \overline{C}_s) &= \int_s^{s+ds} \int_{-T}^T \mathcal{N}(\Phi(\gamma, \nu) - \mu_O | 0, \Sigma_T) \Gamma(\gamma, \nu) d\nu d\gamma \\ &= \int_{-T}^T \mathcal{N}(\Phi(s, \nu) - \mu_O | 0, \Sigma_T) \Gamma(s, \nu) d\nu ds. \end{aligned} \quad (29)$$

Plugging this in eq. (23) results in a Volterra integral [32], leading to

$$\begin{aligned} P_{H2}^a(C) &= 1 - \exp\left(-\int_0^1 \int_{-T}^T \mathcal{N}(\Phi(\gamma, \nu) - \mu_O | 0, \Sigma_T) \Gamma(\gamma, \nu) d\nu d\gamma\right) \end{aligned} \quad (30)$$

The problem with this approach is to find a parametrization diffeomorphic to \mathbb{W} , which is generally not trivial.

Consider indeed the naïve parametrization

$$\Phi(s, \theta) = \begin{bmatrix} \mu_{R_x}(s) - \theta \frac{d\mu_{R_y}}{ds}(s) \\ \mu_{R_y}(s) + \theta \frac{d\mu_{R_x}}{ds}(s) \end{bmatrix}. \quad (31)$$

In this case the curve parametrization $\mu_R(s)$ is augmented by the variable θ , which indicates the “off-track” parameter, i.e. the locally orthogonal deviation from $\mu_R(s)$. The boundary of the domain of θ is given by the parameter T , which for the space swept by an object of circular shape amounts to the object radius r (in our case, as the circle is generated by two objects, $r = r_r + r_O$).

Note that eq. (31) is not a diffeomorphic map between the parametrization space and \mathbb{W} , indeed it is only homeomorphic locally in a neighborhood around $T = 0$, unless the trajectory is a straight line. Therefore, whenever $\mu_R(s)$ intersects itself or its curvature is not null, some region of the integration set D_T will be considered multiple times². Due to those issues, the double integral eq. (28) does not always give a good approximation of eq. (25). Besides that, evaluating eq. (28) can still be relatively expensive to compute. These problems spawn from the continuity of the path as, even under (H3), defining

²Equation (28) and eq. (30) only require $\Phi(s, \theta)$ to be differentiable almost everywhere w.r.t. to s and θ .

precisely the infinite set of unions D_T for eq. (25) is, in general, analytically convoluted and computationally challenging.

We refer to the probability approximation computed by the integral eq. (28) with parametrization eq. (31) as *Naïve Set Parametrization Approach*.

IV. CURRENT COMPUTATIONAL APPROACHES

As already discussed in Section I, different approaches in literature dealt with the estimation of collision probability along a continuous path. Here we retrace how Grid-Based and Stage-Wise approximation methods deal with this problem, highlighting some of their drawbacks.

A. Grid-Based Methods

In their simplest form, Bayesian Grids [20] consist in a tessellation of the environment and a set of Random Variables \mathbf{m} . Each element of \mathbf{m} , m_i , is a binary Random Variable representing the occupancy of the tile in the discretized space with associated probability $P(m_i) \triangleq P(m_i = 1)$. With an implicit abuse of notation, we will indicate with m_i both the occupancy of the tile, and the tile itself. Assuming the hypothesis, similar to (H1), that each cell forming the grid is independent, enables the real-time capabilities of this approach, as the value of each single cell can be updated without considering the joint probability function of the entire map. Specifically, the quantity updated is the belief (or posterior) probability of occupancy $P(m_i | z_{1:t}, y_{1:t})$, given both the set of the robot’s measurements $z_{1:t} = \{z_1, z_2, \dots, z_t\}$ and the set of its poses $y_{1:t} = \{y_1, y_2, \dots, y_t\}$ up to time t . The value of the cells updates according to Bayes Rule³

$$P(m_i | z_{1:t}, y_{1:t}) = \frac{P(z_t, y_t | m_i) P(m_i | z_{1:t-1}, y_{1:t-1})}{P(z_t, y_t | z_{1:t-1}, y_{1:t-1})}. \quad (32)$$

After each cell is updated at some fixed time t , the independence assumption is used to compute the probability of collision along the path followed by the robot.

Denote the set of the tiles crossed by the robot as \mathbf{m}_c and the collision event $m_i = 1$ as C_i (of which the belief is eq. (32)). Considering independent events, the probability of collision in the grid case is

$$P_g(C) = 1 - \prod_{m_i \in \mathbf{m}_c} (1 - P(m_i | z_{1:t}, y_{1:t})). \quad (33)$$

As noted by [21] and others, one of the issues of this approach is that in no way the area of the tiles is taken into consideration, as the belief probability gets updated using only the sensor readings at time t . Therefore, the discretization resolution influences the probability of collision computed by the method, as shown in fig. 5. Even if we circumvent this issue and compute $P(m_i)$ instead of its belief eq. (32), the independence assumption and the multiplicative formula eq. (33) would lead to incorrect conclusions, as we show numerically in Section VII.

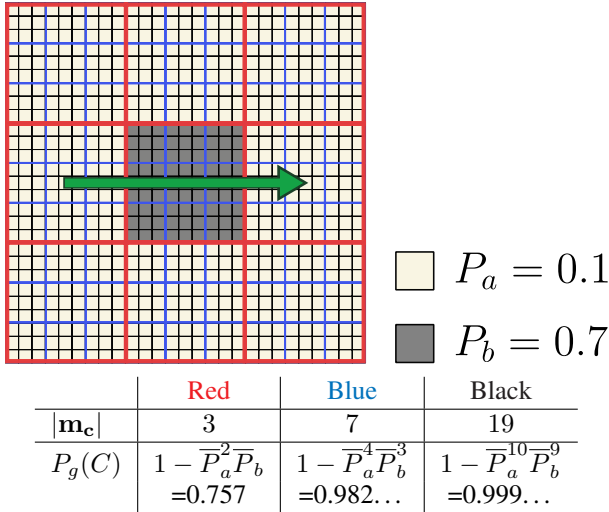


Figure 5: Example of discretization choice effect on the computed probability by grid-based methods. The path crossed by the robot (green) lives in \mathbb{R}^2 , and 3 distinct tessellations of the environment are given (red, blue, black). The robot sensors measure different probability values eq. (32) for the cells depending on the image's color. The probability computed using eq. (33) assumes different values depending on the discretization, although the underlying environment is the same. Indeed, the probability changes as a function of the cardinality of the set \mathbf{m}_c .

B. Stage-wise Probability Estimation Methods

Chance constraints are a popular framework used in optimization to address the risk of collision. Specifically, chance constraints are inequalities involving probabilities in the form of $P(C) \leq \delta$.

To convert individual chance constraints to scalar inequalities, either an approximation or a bound on the probability of the event can be used. The authors of [10] consider both the obstacle and the robot as normally distributed objects of spherical shape and give an approximation of the probability of collision eq. (15) as

$$P(C) \approx V_S \frac{1}{2\pi \sqrt{\det(\Sigma_T)}} \exp -\frac{1}{2}(\mu_R - \mu_O)^T \Sigma_T^{-1} (\mu_R - \mu_O), \quad (34)$$

where the variables used are the ones introduced in Section II, and V_S is the area of the combined disk, in \mathbb{R}^2 $V_S = (r_o + r_r)^2 \pi$. The method amounts to taking the value of $\mathcal{N}(x|0, \Sigma_T)$ at $x = \mu_R - \mu_O$, the center of the combined disk obtained as described in section II, and multiplying it for V_S . While this approximation is efficiently evaluated and, as such, can be implemented in dynamic planning methods [33], its value is not assured to upper-bound the actual probability. An alternative to this is proposed in [17] where an optimization problem is set up to compute x_{max} , the point inside the combined disk that maximizes $\mathcal{N}(x|0, \Sigma_T)$, and then multiplying it for V_S : this always bounds the true probability from above, as shown in fig. 6b.

Whenever the event C (i.e. the collision along a continuous path) to be bounded in probability is constituted by the

³In practice, the log-odds form of this relation is used, as it has better computational performances.

interaction of multiple events, joint chance constraints are used. At the foundation of this framework lies the idea of approximating the probability of collision eq. (20) along a continuous path with the probability of the union of some discretized set of configurations $\mathbb{I} \subset \mathbb{S}$ (waypoints) along the path,

$$P(C) \approx P \left(\bigvee_{i \in \mathbb{I}} C_i \right). \quad (35)$$

A bound on the right-hand side of eq. (35) is called Joint Chance Constraint. Being Joint chance constraints computationally unapproachable, even in a discrete scenario, relaxation techniques have been developed. Most of these techniques rely on Boole's Lemma eq. (36),

$$P \left(\bigvee_{i \in \mathbb{I}} C_i \right) \leq \sum_{i \in \mathbb{I}} P(C_i), \quad (36)$$

which over-bounds the probability of the union of the events with the sum of their individual probabilities. We refer to this method as *Stage-Wise Approximation*.

Unfortunately, eq. (35) does not tell how its two sides relate, meaning that the bound on $P \left(\bigvee_{i \in \mathbb{I}} C_i \right)$ could be invalid for $P(C)$. Indeed if the discretization chosen is too sparse, then the left-hand side of eq. (36) will describe only a subset of the wanted event set, and the probability computed could be a lower approximation of the true value $P(C)$, as there is no accounting of the possibility of a collision happening between waypoints. Conversely, by choosing an excessively dense discretization, the gap between the bound and the true value of the probability grows, as shown in fig. 6a.

In practice, this approach tends to be very conservative. When used for trajectory optimization, it rejects possibly feasible configurations [8].

V. RISK DENSITY

Following the analysis of collision probability along a continuous path in Section III, we investigate how the seemingly very different assumptions (H2) and (H3) relate.

Indeed consider the sensitivity to the parameter T , denoting the bounds of the variable θ , of both eq. (28) and eq. (30) with parametrization eq. (31):

$$S_r^{H2}(\mu_R, \overline{T}) := \left. \frac{dP_r^a}{dT} \right|_{T=\overline{T}}, \quad (37)$$

$$S_r^{H3}(\mu_R, \overline{T}) := \left. \frac{dP_r^a}{dT} \right|_{T=\overline{T}}. \quad (38)$$

Notice the explicit dependence of eq. (37) and eq. (38) on the trajectory under scrutiny $\mu_R(s)$ and the dimensional parameter T , as their knowledge implies the parameterization eq. (31).

Lemma 4. *The sensitivity under (H2) and under (H3) are equivalent in $T = 0$, i.e.*

$$S_r^{H2}(\mu_R, 0) = S_r^{H3}(\mu_R, 0) \quad (39)$$

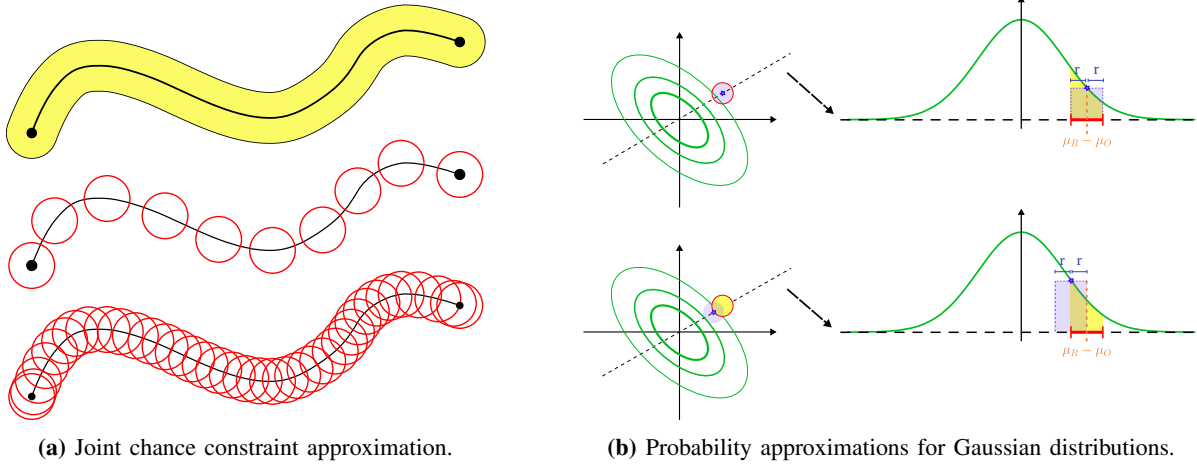


Figure 6: Left: Example of under and over discretization of a continuous path using Boole’s Lemma. Red circles represent the considered robot configurations. The swept area D_T , in yellow, is misrepresented, whether by selecting a set of configurations that is too sparse, leaving out much of the event, or too dense, parametrizing intersections multiple times. Right: Depiction of the approaches used by authors of [10] (top) and [16] (bottom) to approximate Gaussian chance constraints. The boundary of the robot is in red. The approximation integration set is shaded in purple, while the true probability is in yellow.

Proof. The risk sensitivity $S_r^{H2}(\mu_R, \bar{T})$ and $S_r^{H3}(\mu_R, \bar{T})$ can be computed by the Liebniz Integral rule as

$$S_r^{H3}(\mu_R, \bar{T}) = \int_0^1 (\mathcal{N}(\gamma, \nu) \Gamma(\gamma, \nu)) \Big|_{\nu=\bar{T}} d\gamma + \int_0^1 (\mathcal{N}(\gamma, \nu) \Gamma(\gamma, \nu)) \Big|_{\nu=-\bar{T}} d\gamma, \quad (40)$$

$$S_r^{H2}(\mu_R, \bar{T}) = S_r^{H3}(\mu_R, \bar{T}) \exp \left(- \int_0^1 \int_{-\bar{T}}^{\bar{T}} \mathcal{N}(\gamma, \nu) \Gamma(\gamma, \nu) d\gamma d\nu \right), \quad (41)$$

where $\mathcal{N}(\gamma, \nu) := \mathcal{N}(\Phi(\gamma, \nu) - \mu_O | 0, \Sigma_T)$. In $T = 0$, $\Gamma(\gamma, 0) = |d\mu_R(s)/d\gamma|$, and the preceding integrals both evaluate to

$$2 \int_0^1 \mathcal{N}(\mu_R(\gamma) - \mu_O | 0, \Sigma_T) \left| \frac{d\mu_R}{d\gamma} \right| d\gamma,$$

where $|\cdot|$ is the 2-norm. \square

The result is a functional taking a path parametrization μ_R and giving a positive scalar as an output. We refer to this map as the *Risk Density* along μ_R , namely

$$r_d(\mu_R(\cdot)) = 2 \int_0^1 \mathcal{N}(\mu_R(\gamma) - \mu_O | 0, \Sigma_T) \left| \frac{d\mu_R}{d\gamma} \right| d\gamma. \quad (42)$$

Within the limits of the parametrization choice eq. (31), lemma 4 indicates that (H2) and (H3) converge in the limit to the same formulation. The sensitivity of the collision probability to small changes in the robot-obstacle dimensions is the same in apparently very different conditions, i.e. the case when only the initial position of the robot/obstacle is uncertain, or when the obstacle can appear randomly in front of the robot.

Besides the interesting theoretical result that the concept of *Risk Density* reconciles two very far points in the range of possible assumptions about collision interaction, we argue that

eq. (42) also has more practical uses. In the rest of this paper we will show how well an approximation in the form

$$P_a(C, T) \simeq r_d(\mu_R(\cdot))T, \quad (43)$$

can estimate collision probabilities.

Remark. Notice how our derivation assumes a 2D Euclidean workspace and limits the robot’s transformations to translations. The assumption on the workspace dimensions is for simplicity sake and 3D formulations of eq. (28), eq. (30), eq. (39) and eq. (43) are obtained in appendix A. We leave the analysis of the collision probability with rotations to future work.

Risk Density for multiple Obstacles

To compute the equivalent of eq. (42) for an environment where multiple obstacles O_i live, we first introduce an assumption on the interaction between the collision events w.r.t. different obstacles. Namely we assume

$$P(C|O_i) \perp\!\!\!\perp P(C|O_j), \forall i \neq j, \quad (44)$$

i.e. that whether the robot collides with an obstacle or not does not affect the probability of collision with another obstacle. Equation (44) let us write the total probability of collision w.r.t. a set of obstacles \mathbb{O} as⁴

$$\begin{aligned} P(C) &= 1 - \prod_{O_i \in \mathbb{O}} (1 - P(C|O_i)) \\ &= 1 - \prod_{i \in \text{ind}(\mathbb{O})} \left(1 - \left(1 - \exp \left(- \int_{-T_i}^{T_i} \int_0^1 \mathcal{N}_i(\gamma, \nu) \Gamma_i(\gamma, \nu) \gamma \nu \right) \right) \right) \\ &= 1 - \prod_{i \in \text{ind}(\mathbb{O})} \exp \left(- \int_{-T_i}^{T_i} \int_0^1 \mathcal{N}_i(\gamma, \nu) \Gamma_i(\gamma, \nu) \gamma \nu \right) \end{aligned} \quad (45)$$

⁴We derive here the expression for multiple obstacles under (H2), but the procedure remains unvaried under (H2).

where T_i are the radii of O_i , while $\mathcal{N}_i(\gamma, \nu) = \mathcal{N}(\Phi(\gamma, \nu) - \mu_{O_i} | 0, \Sigma_{T_i})$ and $\Gamma_i(\gamma, \nu) = |\det(\nabla \mathcal{N}_i)|$. Define the vector $\mathbb{T} = [T_1, \dots, T_i, \dots]^\top$ and the shorthand

$$\bar{P}_i := \exp\left(-\int_{-T_i}^{T_i} \int_0^1 \mathcal{N}_i(\gamma, \nu) \Gamma_i(\gamma, \nu) \gamma \nu\right). \quad (46)$$

Taking the sensitivity of eq. (45) w.r.t. \mathbb{T} is trivial by using the derivative product rule

$$\begin{aligned} \nabla_{\mathbb{T}}(45) &= -\sum_{i \in \text{ind}(\mathbb{O})} \left(\left(\prod_{j \in \text{ind}(\mathbb{O}), j \neq i} \bar{P}_j \right) \nabla_{\mathbb{T}} \bar{P}_i \right) \\ &= -\sum_{i \in \text{ind}(\mathbb{O})} \left(\left(\prod_{j \in \text{ind}(\mathbb{O}), j \neq i} \bar{P}_j \right) \left[0, \dots, 0, \frac{d\bar{P}_i}{dT_i}, 0, \dots \right]^\top \right). \end{aligned} \quad (47)$$

Evaluating eq. (47) in $\mathbb{T} = \bar{0}$, as each $\bar{P}_j(T_j = 0) = 1$ and $\frac{d\bar{P}_i}{dT_i} = -rd_{O_i}(\mu_R)$, results in the vector

$$rd_{\mathbb{O}}(\mu_R) = \begin{bmatrix} \vdots \\ rd_{O_i}(\mu_R) \\ \vdots \end{bmatrix}. \quad (48)$$

Moreover we can recover the familiar approximation eq. (43) as

$$P_a(C, \mathbb{T}) = \sum_{i \in \text{ind}(\mathbb{O})} rd_{O_i}(\mu_R) T_i = rd_{\mathbb{O}}(\mu_R)^\top \mathbb{T}. \quad (49)$$

VI. NUMERICAL COMPARISON

Setup

To analyze the proprieties of the proposed function, we introduce a simple case study, compatible with the assumptions of Section II and (H3), which, despite its simplicity, captures some of the problem richness.

A robot vehicle shaped as a disk of radius $r_r = 0.05$, must navigate a room with a flat floor with a round obstacle of radius $r_o = 0.05$, roughly located in the middle of the room. Both the robot initial position and the obstacle location are known with some uncertainty that we can model as two independent Gaussian distributions $N_R \sim \mathcal{N}(0, \Sigma_R)$, $N_O \sim \mathcal{N}(0, \Sigma_O)$. We want to evaluate the collision probability along three different paths μ_A , μ_B , and μ_C , all starting from the origin x_0 and finishing $x_F = \begin{bmatrix} 5 \\ 0 \end{bmatrix}$, while the nominal position of the obstacle is $\mu_O = \begin{bmatrix} 5/2 \\ 0 \end{bmatrix}$. The first trajectory, μ_A , is a straight line crossing the nominal position of the obstacle, μ_B and μ_C are parabolas of which the former is designed to graze the obstacle in the nominal position, while the latter passes close to it albeit always staying further than r . We look at how the probability value, computed with different approaches, varies with regard to the magnitude of the covariance matrix Σ_T . To look at the variation of this parameter we multiply a identity matrix by a scalar value σ so that $\Sigma_T = I \cdot \sigma$; this parameter takes 10 values spaced on a logarithmic scale in the range $(10^{-3}, 1)$. We emphasize that Σ_T is a simulation parameter fixing the combined robot-obstacle uncertainty. The choice of its value, in the context of this experiment, is arbitrary and imposes an isotropic uncertainty.

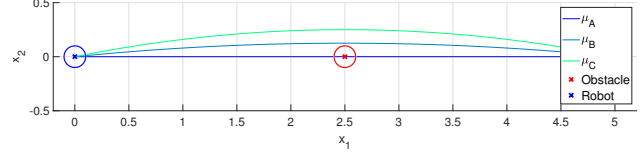


Figure 7: Case in study: nominal case. Close-up of the set-up with the three parabolic trajectories μ_A, μ_B, μ_C . The trajectories are parametrized as $\left\{ \begin{bmatrix} s \\ 0 \end{bmatrix}, \begin{bmatrix} -s^2 - s/2 \\ s - s^2 \end{bmatrix}, \begin{bmatrix} s \\ s - s^2 \end{bmatrix} \right\}$. The initial condition x_0 is in the origin, while $x_F = \begin{bmatrix} 5 \\ 0 \end{bmatrix}$. The robot and the obstacle are disks with radius $r_{r/O} = 0.05$.

Ground Truth: To compute what we take as the ground truth, we perform a Monte Carlo simulation, consisting of 10^4 trials, for each of the 30 cases in scrutiny. At the start of each trial a random sample μ_0^* is taken from $\mathcal{N}(x|\mu_O, \Sigma_T)$ ⁵, representing the actual position of the obstacle for the simulation. Afterwards, given a discretization resolution ds for the curvilinear parameter s , at each step if $|\mu_i(s) - \mu_0^*| \leq r_r + r_o$ then the simulation has stopped and a collision is registered. The steps of this computation are fully enumerated in Appendix A (algorithm 3), where we also include procedures for other assumptions. From the Monte Carlo simulation results we compute the probability ground-truth $P_T(C)$ for each of the inquired scenarios.

We compute the Monte Carlo simulation for μ_B under H1 H2 H3 to make their differences apparent. In this experiment the covariance parameter σ lives in a logarithmic range $[10^{-3}, 10^0]$ and the radius r of the combined object is varied linearly in $[0.1, 1]$.

1) *Naive Set Parametrization Probability Estimation:* The approximation given by eq. (28), using the parametrization (31), is computed for all the considered trajectories.

2) *Grid-Based Probability Estimation:* We evaluate the approximation given by the multiplicative formula eq. (33) in various scenarios. The set of cells $\mathbf{m}_c := \{m_1, \dots, m_N\}$ which the robot intersects is obtained by rasterizing D_T on the grid.

As it was observed, the belief value eq. (32) associated to each cell must be corrected to take the size of the cell into account. We can do so by letting

$$P(C_{m_i}) = \int_{\mathcal{D}(m_i)} \mathcal{N}(x|\mu_O, \Sigma_T) dx, \quad (50)$$

where $\mathcal{D}(x)$ gives the dominion of the cell. This formula obviously accounts for the area of the tiles. Then eq. (33) is rewritten as

$$P_g(C) = 1 - \prod_{m_i \in \mathbf{m}_c} (1 - P(C_{m_i})) \quad (51)$$

In addition to the variation of the covariance matrix and the different trajectories, we also consider different grid resolutions in our benchmark.

⁵via the MATLAB function `mvrnd()`

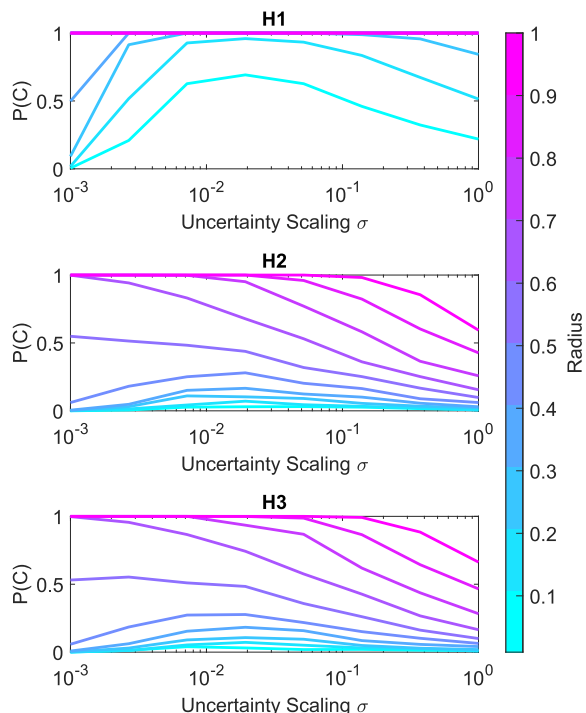


Figure 8: Comparison of Collision Event assumptions. Each plot shows the result of the Monte Carlo probability estimate under different assumptions. The color gradient indicates different radii.

3) *Stage-wise Probability Estimation:* Combining the two approximations used by Chance Constraints, the *Stage-wise approximation* amounts to

$$P_{cc}(C) \approx \sum_{i=1}^N P(C_i) \quad (52)$$

in which each $P(C_i)$ is calculated as in eq. (35). Also, being $P_{cc}(C)$ a probability, we consider the performance of the approximation by saturating it to 1. We also vary the number of waypoints N linearly from 25 to 300.

Risk Density Based Probability Approximation: The approximation we employ is eq. (43) setting $T = r$, namely

$$P_r(C) = rd(\mu_R(s)) \cdot r, \quad (53)$$

where $r = r_r + r_o$ is the combined radius. As it was the case for eq. (52), we saturate the value of eq. (53) to 1.

Assumptions Comparison

The results of the Monte Carlo simulations for the considered assumptions is shown here. The algorithms are detailed in appendix A, the number of trials is set to $N_t = 10^4$, the number of partition of the parameter space $[0, 1]$ is set to $N_s = 10^4$.

In Figure 8, the probabilities given by the trials are shown. We immediately see how the simulation under H1 results in probabilities tending to 1 even for very small radii and high uncertainty values. This shows how H1, due to the fine discretization, is not fit to model this continuous setting.

In H2 and H3 case, while differences are present, the results are comparable. As a consequence, while the following

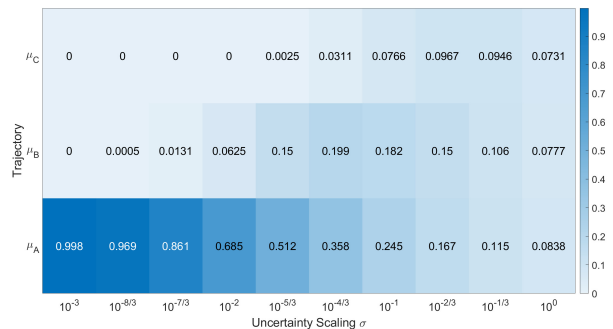


Figure 9: Probability of Collision, Monte Carlo Simulations. The heatmap shows the probability of collision along the trajectories μ_A , μ_B , and μ_C , as a function of increasing values of the position error covariance Σ_T . Each cell is the result of the ensemble of the Monte Carlo Trials for that combination of covariance matrix and trajectory. This heatmap is considered the ground truth.

subsection display results simulated under (H3), eq. (43) could be used also in (H2) case.

Comparison Metric

Denote $M_T \in [0, 1]^{3 \times 10}$ as the matrix containing the ground truth for all the scenarios, and $M_P \in \mathbb{R}_+^{3 \times 10}$ as the matrix containing the same values computed by any of the presented approaches.

The error matrix is defined as

$$M_e = M_T - M_P. \quad (54)$$

The Frobenius Norm $\|\cdot\|_F$ and the maximum element in absolute value $\max(|\cdot|)$ are used to compare the methods outlined in Section VI.

Results

Monte Carlo simulation results are displayed in Figure 9 for all scenarios. The heatmap shows both the trend with respect to σ and the trajectory choice. While μ_A is clearly the riskier trajectory and presents a peak in collision probability for very low values of σ , we see how the probability of collision shows a maximum with respect to the covariance in each path. At higher values of covariance, probability between the trajectories tends to coincide.

The probability approximated by the set parametrization approach eq. (28) is very accurate for the first trajectory, as shown in fig. 10, but quickly degrades and overbounds as the trajectory gets further away and the curvature increases.

The grid-based approximation eq. (51) estimations are shown in fig. 11. In each of the heatmaps, the probability value is shown regarding uncertainty and the path picked. In Figure 12 the Monte Carlo simulation is shown along with the values obtained from the grid-based approach with cell size 2^{-9} . It is apparent that the estimation converges to a specific curve by considering a finer and finer grid, but this value approximates the ground truth poorly.

The heatmaps in Figure 13 present the behaviour of the stage-wise approximation eq. (52). The method tends to be more and more conservative as the number of waypoints N increases.

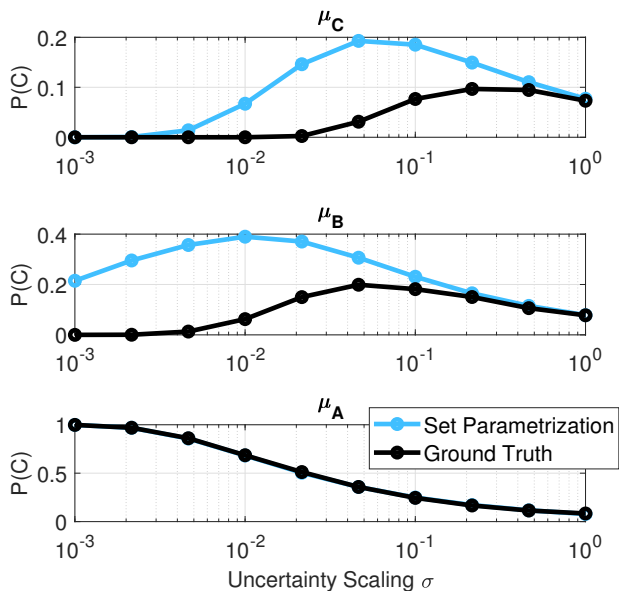


Figure 10: Probability of Collision, Set Parametrization. Values result of the integral eq. (28). We see how, while the parametrization is accurate at evaluating the probability of collision of μ_A , the approximation starts to falter as soon as the curvature of the trajectory is not null.

Moreover, saturation leads to a loss of information about the trajectory, as the estimation predicts a collision regardless of the trajectory. The value of the approximation can either be smaller or larger than the actual probability depending on the number of waypoints, as shown in Figure 14.

The trend of *risk density* eq. (42) considered in isolation is displayed in fig. 15. The behaviour of the approximation eq. (53) is compared to the ground truth given by Monte Carlo in fig. 16.

A summarizing view is given in fig. 17. Here the errors against the ground truth are plotted with regard to σ . The set parametrization approach eq. (28), shown in light blue in fig. 17, is the most accurate in appraising the risk of μ_A , while the discrepancy with the Monte Carlo ground truth is larger the further the path is from the obstacle.

A more detailed comparison is given in table I. The table shows how our approach gives a 12% improvement in the Frobenius norm of the estimation error matrix compared to the stage-wise approximation. The unsaturated values are not included, as is evident how the stage-wise approximation greatly overestimates the actual probability whenever the path in inquiry is “closer” to the obstacle (μ_A).

VII. DISCUSSION

As shown by the simulations, the accuracy of the approaches varies greatly, even in the simple scenario considered above.

All reviewed methods capture the qualitative behavior shown by the Montecarlo simulation, exhibiting a maximum in the probability estimate with respect to the uncertainty scaling for all approaches. However, the parametrized probability integral eq. (28) is not a reliable approximation even for modest curvature values: this happens due to the fact that

the parametrization eq. (31) of the integration set is not an homeomorphic map between $[0, 1] \times [-T, T]$ and \mathbb{W} , leading to an overestimation of the actual probability value. Moreover, the computation is 1 – 2 orders of magnitude slower with respect to other methods.

As mentioned in Section VI, the ground value peak appears at very low values of σ in μ_A 's case. Ideally the peak would be at $\sigma = 0$, the deterministic scenario, since the probability of collision of a nominal path passing through an obstacle whose position is known with 100% certainty. As the path moves away from the obstacle nominal position, the peaks also shift towards higher values: while in the deterministic case the robot would narrowly avoid the obstacle, a higher variance Σ_T favours the collision event.

When the resolution of the cells gets finer, the grid-based method does not converge to the probability predicted by the Montecarlo simulation. This fact is mainly due to the difference between the assumption underlying the grid approach and (H3): the latter assumes the independence of cells, which does not apply to this scenario.

The stage-wise approximation eq. (52) of the probability of collision is fast and, as such, suited to optimization. However, while eq. (34) is not guaranteed to overbound the probability, we observe that for almost every number of waypoints, the result of eq. (52) is a substantial overapproximation of the ground truth. This conservativeness in an optimization setting could lead to categorizing admissible states as unfeasible.

At last, the proposed function eq. (42), coupled with the approximation eq. (53), shows some interesting properties. As no exogenous parameters are included in its computation, we call it *path intrinsic*; namely, the probability eq. (53) is just a functional of the path $\mu_R(\cdot)$ taken by the robot and the combined radius r , while no other tuning knob, such as N , the number of waypoints, or the resolution of a grid, is considered. It could be argued that the r parameter by which the density eq. (42) is scaled in eq. (53) is not the optimal one to estimate the probability of collision. To validate our choice, we obtain r_{opt} by minimizing $\|M_e\|_F$ for an arbitrary choice of the scaling parameter. As shown in table I, the variation in the values of the error is modest and does not justify the need for this optimization.

Curiously, the approximation eq. (53) is more accurate than the integral eq. (28): taking the derivative of eq. (28) at “thickness” 0 rids eq. (53) of the local homeomorphicity issue encountered in eq. (28). Furthermore, the method also seems to be competitive in regard to the accuracy of the approximation, being the least conservative among the considered approaches.

While limited in scope, the experiment also shows that the computational cost of the Risk Density approach is of the same order of magnitude ($\sim \times 2$) as the fastest method (Stage-wise approximation), as shown in table I. This relatively small computational complexity is explained by the fact that our approximation eq. (53) includes only a uni-dimensional integral, which is easily evaluated numerically.

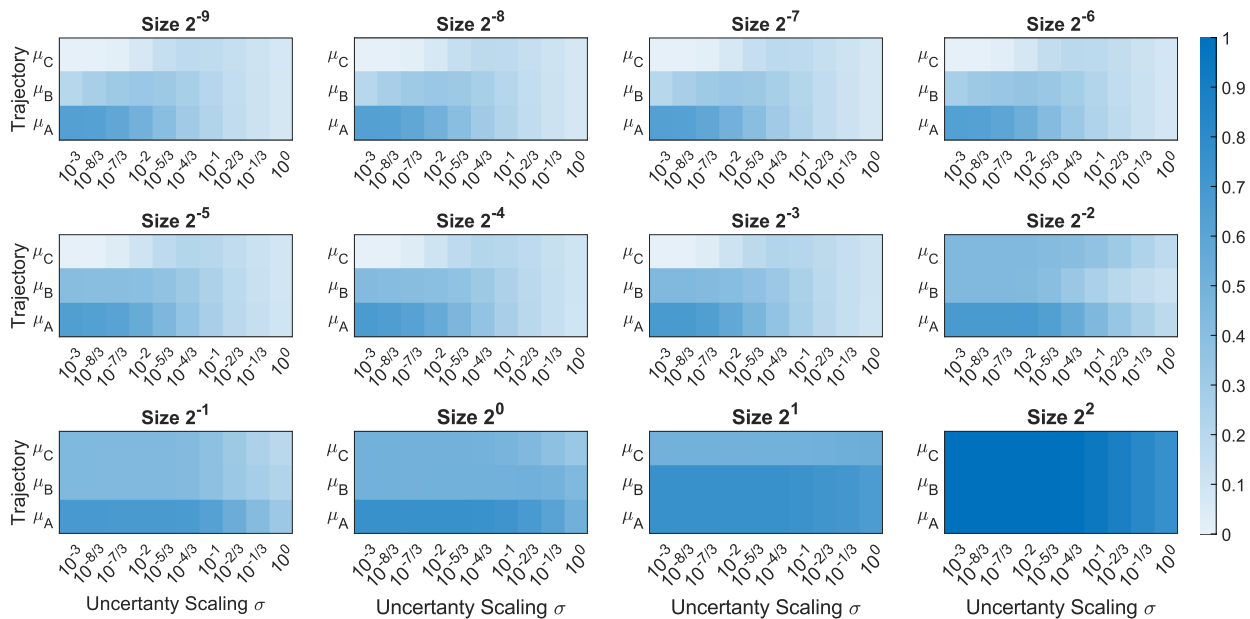


Figure 11: Probability of Collision, Grid based method. The heatmaps show the value of the probability of collision with regard of the size of the square tiling. The probability value associated to each pairing of trajectory and σ converges as the resolution of the grid gets finer.

	Stage-wise ($N = 50$)	Parametrization eq. (31)	Risk density r	$r_{opt}(= 0.1043)$	Grid-based (Size= 2^{-9})	Monte Carlo ($N_T = 10^4$)
$\max(M_e)$	0.2796	0.3438	0.2863	0.2689	0.7754	0
$\ M_e\ _F$	0.649	0.698	0.579	0.545	2.869	0
Comp Time [s]	$(7.2 \pm 2.2) \cdot 10^{-3}$	$(8.7 \pm 0.5) \cdot 10^{-1}$	$(1.3 \pm 0.2) \cdot 10^{-2}$	\sim	380.43*	29 ± 3

Table I: Value of the matrix norm of the ensemble of errors M_P and computation time of considered methods. The computation time refers to the execution of the whole set of 30 scenarios. The stage-wise and risk density-based approach errors are from the saturated approximation. The values in the table were obtained by running each method 100 times and computing the mean time and its standard deviation. All the simulations were run on a modern laptop with Matlab 2022b on an Intel i7-12700H with 32GB of Ram. *We include the computation time for the grid-based computation for completeness, but our simulation introduces complexity that would not be present in a standard implementation.

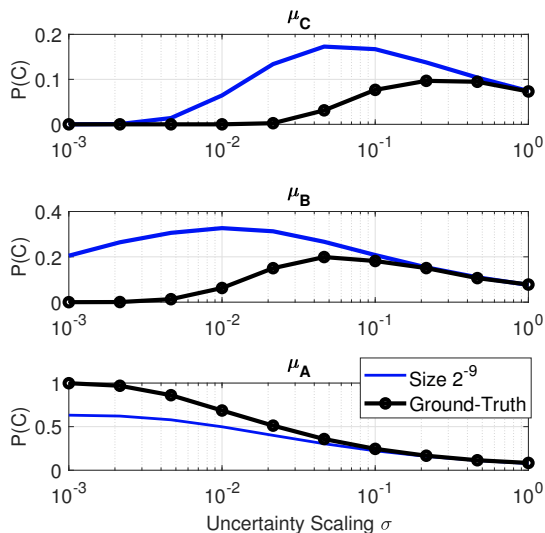


Figure 12: Probability of Collision, Grid based method - tile size 2^{-9} . As the resolution gets finer, the grid-based approach converges to a value, which however is not the amount result of Monte Carlo simulation.

VIII. RISK DENSITY AND THE SENSITIVITY OF COLLISION PROBABILITY

As shown in section VI, risk density can be used to give an approximation of the collision probability when the position of the robot and the obstacle are uncertain. We now depict another situation in which eq. (42) is useful. Let us assume that we have already computed the probability of collision very accurately (e.g. through a long running MC simulation) for an environment we know the dimensions of very well. We call this estimate of the collision probability $P_M^{(i)}$ and its associated dimensional parameter T_i . Assume now that the dimension of the robot and/or the obstacle, i.e. the environment, changes, while the trajectory followed by the robot, μ_R , is unvaried. The previously computed estimate of the collision probability is now invalid, but computing the collision probability $P_M^{(i+1)}$ would imply a hefty computational cost. To ameliorate this issue, we can use the risk density based approximation eq. (43).

A first order approximation of $P_M^{(i+1)}$ given by the sensitivity is

$$P_M^{(i+1)} \approx P_M^{(i)} + S_r^{Hi}(\mu_R, T_i) \cdot dT_i, \quad (55)$$

where Hi stands for either $H2$ or $H3$. We can obtain a similar relation by exploiting the collision probability approximation given by the risk density. Explicitly, when both the probabilities $P_M^{(i+1)}$ and $P_M^{(i)}$ are approximated by eq. (43), the following

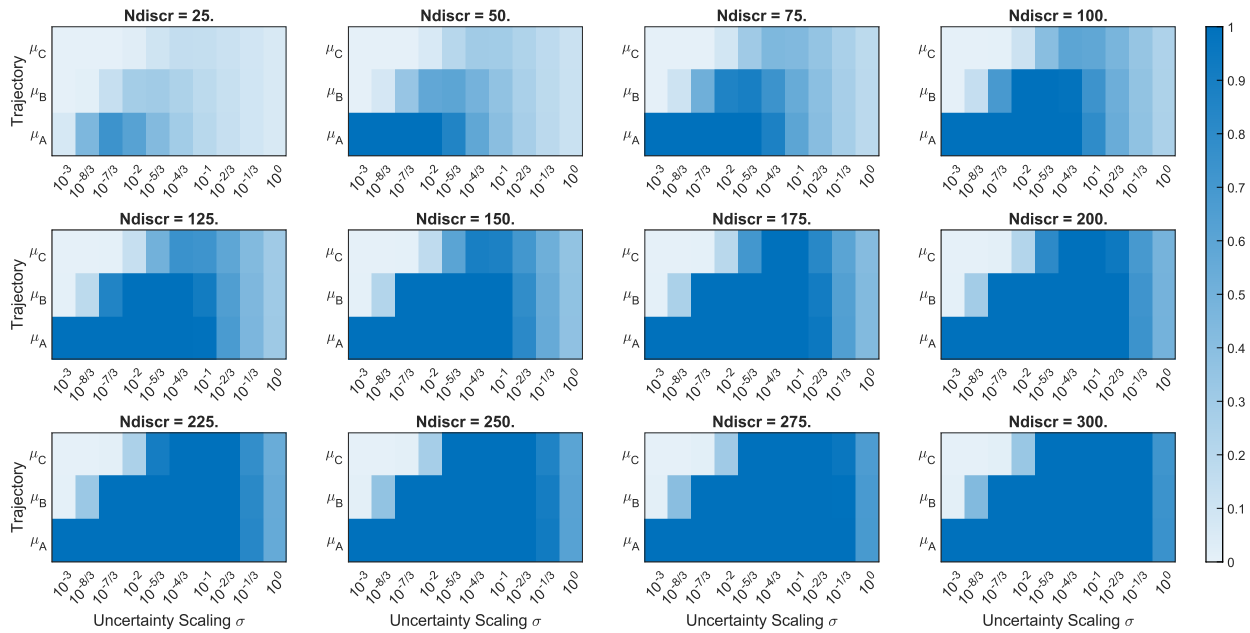


Figure 13: Probability of Collision, Stage-wise method. Result of the approximation using eq. (52). The number of waypoints, in which the approximation is computed, is varied. The values computed are ceiled at 1. We see how the approximation is not informative after a certain number of waypoints as it always predicts a collision even in the safest of cases.

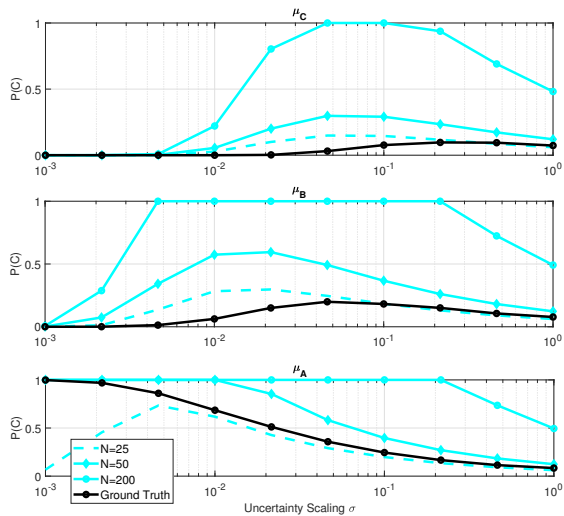


Figure 14: Probability approximation, Stage-wise approximation. Values result of eq. (52), for some selected number of waypoints N , compared against Monte Carlo simulation. While usually this approach overbounds, notice how when $N = 25$ the probability of μ_A is lower than the actual value.

can be written

$$P_M^{(i+1)} \approx P_M^{(i)} + r_d(\mu_R) \cdot d_{T_i}, \quad (56)$$

where $d_{T_i} = (T_{i+1} - T_i)$. While the formulation eq. (55) should in principle give a better estimation, it also requires to compute an integral for each evaluation, i.e. eq. (40) for every CP at a different T_i , while eq. (56) requires to compute just once a uni-variate integral, the risk density eq. (42).

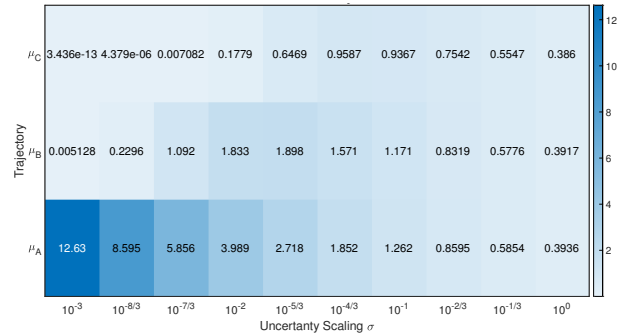


Figure 15: Risk Density. Behaviour of eq. (42) w.r.t. uncertainty scaling and path chosen. While the vales shown are not probabilities, the behavior with respect to σ is maintained.

Numerical Validation Setup

To explore how the proposed approximation eq. (56) performs, we compute its value and the result of a MC simulation (considered as ground truth) in a slightly modified version of the setup introduced in Section VI. We maintain the choice of paths and the range of σ , albeit lowering the resolution, while we impose the combined disk radius r to vary logarithmically in the range $[10^{-2}, 1]$: accordingly the value of d_{T_i} at each index will be $r_{i+1} - r_i$.

Discussion of Results

The graph Figure 18 shows a comparison of the result of eq. (56) against the ground truth, while the tables table II table III display both the absolute error and the relative absolute error between the two, i.e. $e_a = |P_M^{(i+1)} - P_M^{(i)} + r_d(\mu_R) \cdot d_{T_i}|$ and $e_r = e_a / P_M^{(i+1)}$.

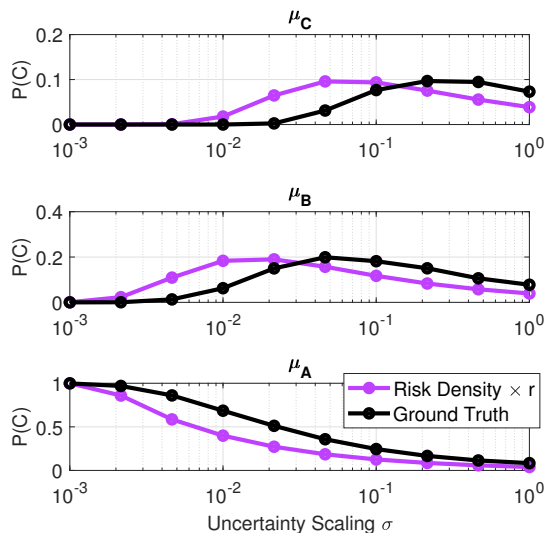


Figure 16: Probability of Collision, Risk Density. Behaviour of the proposed approximation eq. (42) against Monte Carlo simulation. Notice how the purple lines have the same “shape” of the heatmap shown in fig. 15, as these two graphs differ only by the multiplication factor r , as in eq. (53).

$\mu \setminus \sigma$	10^{-3}	10^{-2}	10^{-1}	1
μ_A	2.33 1.25 [%]	2.63 1.27 [%]	2.23 1.26 [%]	1.23 0.57 [%]
μ_B	9.96 3.15 [%]	0.54 0.75 [%]	2.21 1.43 [%]	1.33 0.72 [%]
μ_C	10.00 1.36 [%]	7.88 1.56 [%]	2.22 1.39 [%]	1.06 0.49 [%]

Table II: Mean absolute error w.r.t. the radius for eq. (56) (Blue) and eq. (55) (Yellow).

We see how the proposed approximation follows the ground truth generally well with few exceptions, as both the mean errors e_a and e_r , are relatively low, making the approach attractive even in comparison to eq. (55): Table II show lower error values for eq. (55) in all but few cases, but the differences are not drastic and there is additional computational cost required. The limitations of the approach show up in the case in which the trajectory is far from the obstacle relative to the covariance scaling σ , e.g. in the set of pairs $\{(\mu_B, 10^{-3}), (\mu_C, 10^{-3}), (\mu_C, 10^{-2})\}$, but while the relative error e_r is high, the absolute one is limited. The reason lies in the fact that the risk density eq. (42) in these cases evaluate very close to 0 and eq. (56) output is very close to $P_M^{(i)}$, shown as an apparent shift of the graphs in fig. 18.

IX. TRAJECTORY OPTIMIZATION

To better explore the applicability of the proposed approach, in this section we show how eq. (43) can be used in an open-loop trajectory optimization setting.

As already explored in section V, consider the set of obstacles \mathbb{O} , each O_i with its associated radius T_i and distribution \mathcal{N}_i .

$\mu \setminus \sigma$	10^{-3}	10^{-2}	10^{-1}	1
μ_A	3.09 1.56 [%]	8.81 1.95 [%]	4.15 2.64 [%]	4.78 3.69 [%]
μ_B	45.97 32.51 [%]	2.26 2.37 [%]	4.36 3.08 [%]	4.23 3.26 [%]
μ_C	18.63 9.95 [%]	22.56 8.78 [%]	4.68 3.56 [%]	5.01 4.14 [%]

Table III: Mean relative absolute error w.r.t. the radius for eq. (56) (Blue) and eq. (55) (Yellow).

Denote as \mathbb{T} the vector of the obstacles’ radii and $rd_{\mathbb{O}}$ the vector of all the risk densities eq. (42) computed for each obstacle. The probability estimation is then given by

$$P_a = rd_{\mathbb{O}} \cdot \mathbb{T}. \quad (57)$$

We give two examples of how this formulation can be used in an optimization setting.

Setup

A robot is to plan a trajectory γ to reach a point hidden behind two “L” shaped corners, while keeping its probability of collision under a certain value.

The trajectory is parametrized as a Bezier curve of the 4th order $\gamma(s, x_c) : \mathbb{S} \times \mathbb{R}^{2 \times 5} \rightarrow \mathbb{R}^2$, of which we optimize the control points x_c to minimize the length of the curve. The obstacles are decomposed in small disks, $r = 0.1$, each distributed normally around their nominal position with identical covariance $\Sigma_i = \sigma \cdot I$. The same setting is investigated under different σ to analyze the effect of varying uncertainty on the optimization.

The optimization problem takes then the following form.

$$\min_{x_c} \int_0^1 \left| \frac{d\gamma}{ds} \right| ds \quad (58)$$

s.t.

$$P_a(x_c) \leq c_{max}$$

$$\gamma(0, x_c) = x_0$$

$$\gamma(1, x_c) = x_F$$

The constrained problem is implemented as unconstrained through the use of a logarithmic barrier function [34] for the first constraint, i.e. an additional term $-\log(c_{max} - P_a(x_c))$ is added to the objective function. In this case we have set $c_{max} = 0.2$. This formulation has been consequently discretized, with $N_d = 300$, and optimized using the `fminunc` function in MATLAB. Each optimization iteration, one for each value of σ , is initialized by a fixed feasible configuration of x_c . To compare the efficacy of this method, both a Monte Carlo simulation with $N_M = 10^4$ trials, and eq. (52)⁶ are computed on the optimized paths.

Results

From Figure 19 we see how the estimate given by eq. (57) is always underestimating the actual probability, while eq. (52) overestimates the collision probability in all but one case. The table table IV shows the error $E_P = P_{est} - P_M$ and the relative error $E_R = E_P / P_M$ respective to the Monte Carlo simulation. We see how the mean of $|E_P|$ and $|E_R|$ are both significantly lower in eq. (57) case. In the individual scenarios our method produces a worse estimate in the absolute value only in the first cases, $\sim \times 2.3$ worse, while doing $\sim \times 1.24 - 26$ better in all other cases. Each iteration was optimized to tolerance in $\sim 0.3s$. It is to note however that our method finds unfeasible solutions,

⁶The summation index set in this case is the cartesian product of the obstacle indexes and the discretization steps.

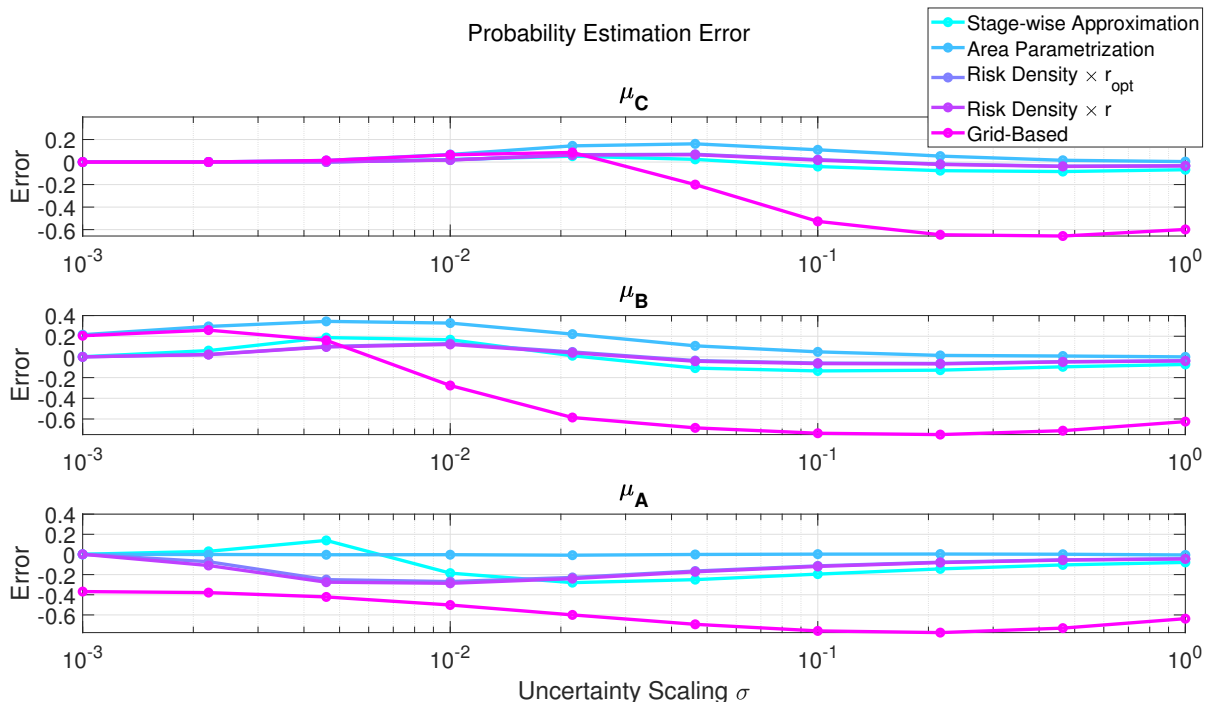


Figure 17: Errors against the Monte Carlo simulation. The error is given in the $[-1, 1]$ range: if the value plotted is positive, there is an overestimation of the probability, conversely, a negative value denotes an underestimation. The stage-wise approximation error shown is computed while fixing N , the number of waypoints, to 50. In the chart we show both the probability estimated by using as a factor r and r_{opt} .

σ	10^{-3}	$10^{-25/9}$	$10^{-23/9}$	$10^{-21/9}$	$10^{-19/9}$	$10^{-17/9}$	$10^{-15/9}$	$10^{-13/9}$	$10^{-11/9}$	10^{-1}	$\mathbb{E}[E_R]$
E_R [%] RD	-64.45	-36.39	-19.75	-11.24	-7.28	-4.85	-4.14	-4.86	-10.91	-18.51	16.54
E_R [%] SW	27.99	45.78	50.10	44.50	33.46	21.41	9.49	-3.03	160.37	152.77	64.48
σ	10^{-3}	$10^{-25/9}$	$10^{-23/9}$	$10^{-21/9}$	$10^{-19/9}$	$10^{-17/9}$	$10^{-15/9}$	$10^{-13/9}$	$10^{-11/9}$	10^{-1}	$\mathbb{E}[E_P]$
E_P [%] RD	-98.99	-97.55	-93.91	-86.12	-73.85	-56.74	-43.41	-36.91	-100.00	-100.00	80.78
E_P [%] SW	42.99	122.74	238.23	340.98	339.34	250.42	99.55	-23.02	1469.93	825.33	491.77

Table IV: Error and Relative Error w.r.t. Monte Carlo simulation for eq. (57) (RD) and eq. (52) (SW). Negative numbers indicate an underestimation of probability. Values in red indicates an actual infeasibility of the trajectory while those in orange indicates feasible trajectories that would have been mischaracterized. Means are computed considering also values not shown in the tables. The maxima are boldened.

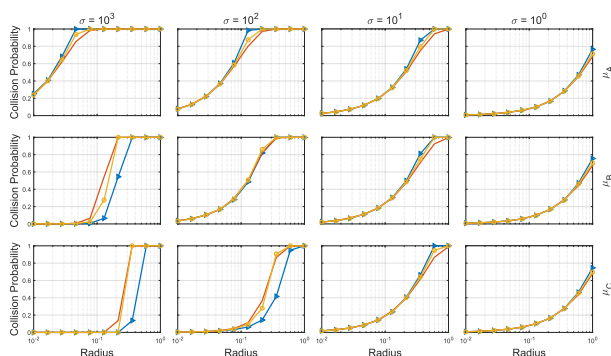


Figure 18: Comparison of MC ground truth against approximations. The graphs show the CP estimate against the radius' dimension. The MC ground truth is showed in Red, while the approximations are depicted in Blue eq. (56) and Yellow eq. (55). The grid is disposed to make the scrutinized pairing of path and σ explicit.

highlighted in red in table IV, while eq. (52) mischaracterize potentially feasible paths, in orange.

Figure 19 shows results consistent with the analysis in Section VII. While the optimization finds trajectories that are

very close to the nominal position of the obstacles while σ is low, intermediate values of the parameter lead to trajectories that are “further away” from the obstacles and higher values result in straight paths. We suppose that this is due to the same peaking phenomenon we have discussed about the probability estimates in Section VII. When the uncertainty is sufficiently low, the optimization is lead to avoid the obstacles. However, when the uncertainty parameter σ is high enough, the obstacles distributions widen to resemble a uniform distribution. Consequently, the probability of collision P_a when circumventing obstacles becomes comparable to that of taking a straight path, which is then preferred. This phenomenon is illustrated in the second plot from the right in Figure 19. When the change of behaviour happens, the probability estimate of the optimized path, in light blue, is roughly equal to the one, in black, of the starting path: the prominent part of P_a is given by the initial and final position and moving x_c in any direction does not lower P_a significantly.

Remark. As highlighted by Figure 19, our method correctly captures the change of behaviour in probability displayed at $\sigma \simeq 0.033$: both the Monte Carlo estimate and eq. (57) trend

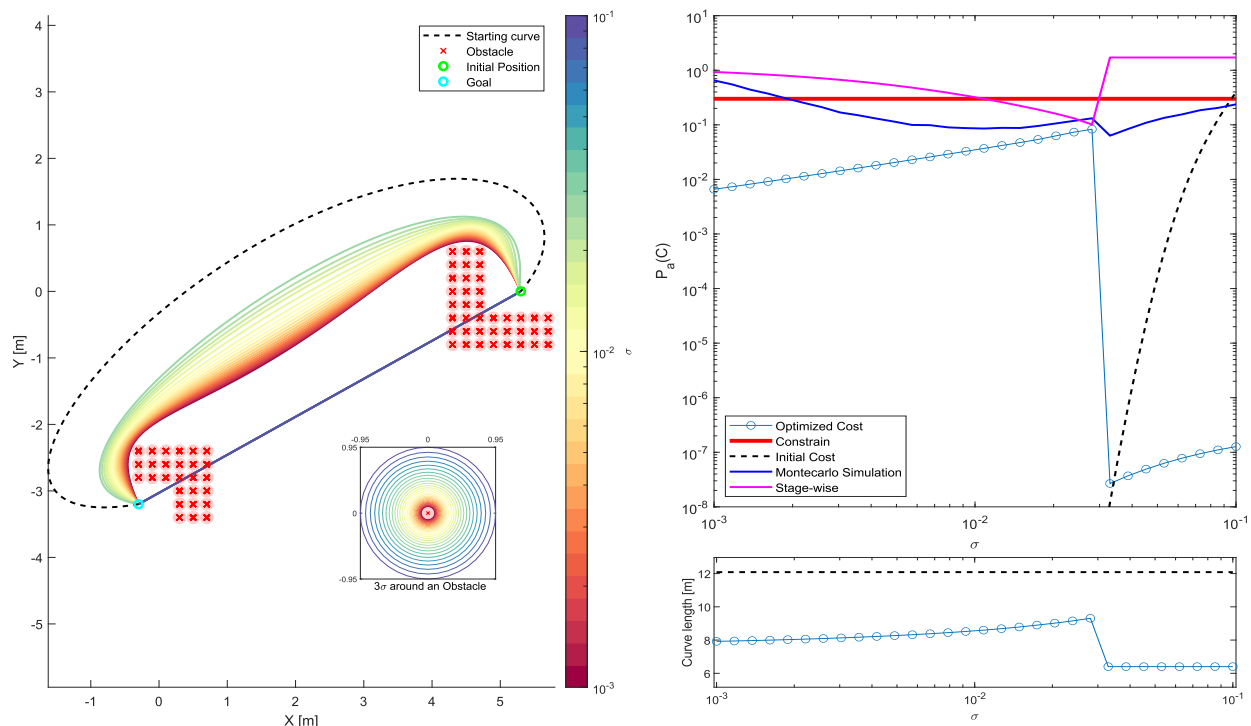


Figure 19: Result of the constrained optimization. Left: Trajectories follow a color gradient highlighting the value of the obstacles’ σ considered. The square in the bottom right shows how large a circle with radius 3-std is. The obstacles are shown in red in their nominal position. Right: Plots detailing the length of the trajectory and the estimated probability for each σ iteration. The probability estimated by a Monte Carlo simulation and by eq. (52) are also shown.

downwards, while eq. (52) captures the opposite behaviour.

X. CONCLUSIONS

This paper presents an analysis of the sensitivity of collision probability to small perturbations in the robot/object dimensions, and introduces the idea of “risk density”. We show that this concept carries over different assumptions about the interplay of collision events, modeling different practical situations and offering a theoretical link between the hypotheses.

The derivation of such approximation starts from analyzing the intersection probability of two uncertain shapes and then generalizing it to a continuous path. After discussing this theoretical property of risk density, we showed how a probability approximation scheme based on it can be applied to the case of a robot moving in a deterministic unknown environment with uncertain initial conditions. We have thus shown how the proposed approximation offers accuracy and performance comparable to or better than other popular probability estimation methods. We have also displayed how the risk density can be used to avoid computing a Monte Carlo simulation when a slight change in environment occurs. The proposed risk-density based approximation does not introduce the need for tuning parameters that are not intrinsic to the problem. Finally we have shown the usefulness of the method in an optimization setting.

Limitations and Future Research

Our numerical comparisons were based on assumption (H3) only, i.e. uncertainty only in the initial condition. While

valid, the assumption is a simplification of the true stochastic nature of the dynamics. Describing the collision event as a stopped process eludes considering the conditioning between states: a better approach would consider that. Our approach to computing collision probability does not currently consider non-Gaussian and non-stationary distributions for the uncertainty. Therefore, further investigation in this regard is warranted. The fact that the *Risk Density* definition coincides between (H2) and (H3) encourages to explore its application to the (H2) case as well. In the context of *Risk Density*, exploring further the theoretical link between (H2) and (H3) and how it can be translated to practical approximations also under other hypotheses is of interest. Moreover, while in this manuscript we have carried out the theoretical derivation of the same method in \mathbb{R}^3 , its efficacy and the further generalizations are to be explored.

Finally the method explored does not factor rotations of the objects in the probability computation. This deficiency is exposed as soon as we do not introduce an overbounding ball and consider directly the robot shape. This issue could be ameliorated by the use of specialized distributions (e.g. Von-Mises or Wrapped Gaussian), or by working directly in a differential geometry setting. We plan to explore these ideas in the future.

XI. ACKNOWLEDGEMENTS

This work was supported by the EU Project DARKO - Dynamic and Agile production Robots that learn and optimize Knowledge and Operations (Grant ID 101017274), Fit4MedRob

- Fit for Medical Robotics Foundation (PNC0000007). Moreover, this work was carried out within the framework of the project ‘‘RAISE - Robotics and AI for Socio-economic Empowerment’’ and has been supported by European Union - NextGenerationEU. The views and opinions expressed are, however, those of the authors alone, and do not necessarily reflect those of the European Union or the European Commission. Neither the European Union nor the European Commission can be held responsible for them.

APPENDIX

A. Risk Density in \mathbb{R}^3

1) *Probability Approximation:* Consider the sphere $b \subseteq \mathbb{R}^3$ bounding the Minkowski difference between the robot and the object shape from outside. The tube swept by the translation of b along the path $\mu_R(s)$ can be parametrized by a function $\Phi(s, t, \theta) : \mathbb{S} \times [0, \bar{T}] \times [0, 2\pi) \rightarrow \mathbb{R}^3$ as

$$\Phi(s, t, \theta) = \mu(s) + t \cdot \left(-\hat{N}(s) \cos(\theta) + \hat{B}(s) \sin(\theta) \right). \quad (59)$$

Here $\hat{T}(s) = \frac{d\mu_R(s)}{ds} / \left| \frac{d\mu_R(s)}{ds} \right|$ is the vector tangent to the curve, $\hat{N}(s) = \frac{d\hat{T}(s)}{ds} / \left| \frac{d\hat{T}(s)}{ds} \right|$ is the normal vector defining one of the base vectors of the plane normal to $\mu_R(s)$, the other given by the binormal vector $\hat{B}(s) = \hat{T}(s) \times \hat{N}(s)$.

Computing the formulas corresponding to eq. (28) and eq. (30) is straightforward and follows the same procedure as in Section III, since lemma 2 and lemma 3 do not depend on the dimension of the space which the sets $D_{RO}(s)$ live in. The resulting expressions are

$$P_{H3}^a(C) = \int_0^{2\pi} \int_0^{\bar{T}} \int_0^1 \mathcal{N}(\gamma, t, \theta) \Gamma(\gamma, t, \theta) d\gamma dt d\theta, \quad (60)$$

$$P_{H2}^a(C) = 1 - \exp \left(- \int_0^1 \int_0^{2\pi} \int_0^{\bar{T}} \mathcal{N}(\gamma, t, \theta) \Gamma(\gamma, t, \theta) dt d\theta d\gamma \right), \quad (61)$$

where $\mathcal{N}(\gamma, t, \theta) := \mathcal{N}(\Phi(\gamma, t, \theta) - \mu_O | 0, \Sigma_T)$, $\Gamma(\gamma, t, \theta) = |\det(\nabla \Phi(\gamma, t, \theta))|$ and the vectors and matrices live in \mathbb{R}^3 .

2) *Risk Density approximation in \mathbb{R}^3 :* Using the Liebnitz integral rule, we write

$$S_r^{H3}(\mu_r, \bar{T}) = \frac{dP_{H3}^a}{dT} = \int_0^{2\pi} \int_0^1 \mathcal{N}(\gamma, \bar{T}, \theta) \Gamma(\gamma, \bar{T}, \theta) d\gamma d\theta \quad (62)$$

and

$$S_r^{H2}(\mu_r, \bar{T}) = \frac{dP_{H2}^a}{dT} = S_r^{H3}(\mu_r, \bar{T}) \exp \left(- \int_0^{\bar{T}} \int_0^{2\pi} \int_0^1 \mathcal{N}(\gamma, t, \theta) \Gamma(\gamma, t, \theta) d\gamma dt d\theta \right). \quad (63)$$

Notice how $\Phi(s, 0, \theta) = \mu_R(s)$, however $\Gamma(s, 0, \theta) = 0 \forall s, \theta$, since the Jacobian matrix of Φ is singular when $t = 0$.

$$\Gamma(s, t, \theta) = \left| \det \left(\begin{bmatrix} \frac{d\Phi}{ds} & \frac{d\Phi}{dt} & \frac{d\Phi}{d\theta} \end{bmatrix} \right) \right| \quad (64)$$

where

$$\frac{d\Phi}{ds} = \hat{T} \left| \frac{d\mu_R}{ds} \right| + t \overbrace{\left(\frac{d\hat{B}}{ds} \sin(\theta) - \frac{d\hat{N}}{ds} \cos(\theta) \right)}^{\textcircled{1}}, \quad (65)$$

$$\frac{d\Phi}{dt} = \hat{B}(s) \sin(\theta) - \hat{N}(s) \cos(\theta), \quad (66)$$

$$\frac{d\Phi}{d\theta} = t \cdot (\hat{N}(s) \sin(\theta) + \hat{B}(s) \cos(\theta)). \quad (67)$$

So the sensitivities in $\bar{T} = 0$ both vanish

$$S_r^{H2}(\mu_r, 0) = S_r^{H3}(\mu_r, 0) = 0. \quad (68)$$

Nevertheless, consider the second order sensitivities

$$S_{r'}^{H2/3}(\mu_r, \bar{T}) = \frac{d^2 P_{H2/3}^a(c)}{dT^2}. \quad (69)$$

By rewriting the determinant inside eq. (64) as a scalar triple product

$$\det(\nabla \Phi) = \frac{d\Phi}{ds} \cdot \left(\frac{d\Phi}{dt} \times \frac{d\Phi}{d\theta} \right). \quad (70)$$

The vector product part of this expression simplifies as

$$\begin{aligned} & \hat{B} \sin(\theta) \times \hat{N} \sin(\theta) t - \hat{N} \cos(\theta) \times \hat{N} \sin(\theta) t \\ & + \hat{B} \sin(\theta) \times \hat{B} \cos(\theta) t - \hat{N} \cos(\theta) \times \hat{B} \cos(\theta) t \\ & = \hat{B} \times \hat{N} \sin^2(\theta) t + \hat{B} \times \hat{N} \cos^2(\theta) t \\ & = -t \hat{T}, \end{aligned} \quad (71)$$

using the anticommutative propriety of the vector product. Moreover, using the Frenet-Serret formulas, $\textcircled{1}$ becomes

$$\textcircled{1} = \left(-\tau(s) \hat{N} \sin(\theta) - (\tau(s) \hat{B} - \kappa(s) \hat{T}) \cos(\theta) \right), \quad (72)$$

where $\kappa : \mathbb{S} \rightarrow \mathbb{R}$ and $\tau : \mathbb{S} \rightarrow \mathbb{R}$ are the curvature and the torsion of μ_R respectively⁷. Being the scalar product bilinear and using again eq. (70), eq. (64) is then

$$\begin{aligned} \Gamma(s, t, \theta) &= \left| \hat{T} \left| \frac{d\mu_R}{ds} \right| \cdot (-t \hat{T}) + t \textcircled{1} \cdot (-t \hat{T}) \right| \\ &= \left| \left(t \left| \frac{d\mu_R}{ds} \right| + t^2 \kappa(s) \cos(\theta) \right) \right|. \end{aligned} \quad (73)$$

We can then write

$$S_r^{H3} = \int_0^{2\pi} \int_0^1 \left(\frac{d\mathcal{N}}{dT}(\gamma, \bar{T}, \theta) \Gamma(\gamma, \bar{T}, \theta) + \mathcal{N}(\gamma, \bar{T}, \theta) \frac{d\Gamma}{dT}(\gamma, \bar{T}, \theta) \right) d\gamma d\theta. \quad (74)$$

When eq. (74) is evaluated in $\bar{T} = 0$ it results in

$$\begin{aligned} S_{r'}^{H3}(\mu_r, 0) &= \int_0^{2\pi} \int_0^1 \mathcal{N}(\gamma, 0, \theta) \frac{d\Gamma}{dT}(\gamma, 0, \theta) d\gamma d\theta = 8 \\ &= \int_0^{2\pi} \int_0^1 \mathcal{N}(\gamma, 0, \theta) \left| \frac{d\mu_R}{d\gamma} \right| d\gamma d\theta = \\ &= 2\pi \int_0^1 \mathcal{N}(\mu_R(\gamma) - \mu_O | 0, \Sigma_T) \left| \frac{d\mu_R}{d\gamma} \right| d\gamma = \\ &= \pi \cdot rd(\mu_R(\cdot)). \end{aligned} \quad (75)$$

⁷These have an algebraic form given that μ_R is of class C^3 , but their value is of no interest here.

Using eq. (74), we derive

$$S_{r'}^{H2} = \frac{d}{dT}(63) = (S_{r'}^{H3} - (S_{r'}^{H3})^2) \exp\left(-\int_0^{\bar{T}} \int_0^{2\pi} \int_0^1 \mathcal{N}(\gamma, t, \theta) \Gamma(\gamma, t, \theta) d\gamma d\theta dt\right). \quad (76)$$

Finally, in $\bar{T} = 0$ this is

$$S_{r'}^{H2}(\mu_R, 0) = S_{r'}^{H3}(\mu_R, 0) = \pi \cdot rd(\mu_R(\cdot)). \quad (77)$$

Moreover, an approximation similar in nature to eq. (43) is recovered using a second order Taylor approximation

$$P_a(C, T) = rd(\mu_R(\cdot)) \cdot \pi T^2, \quad (78)$$

which makes intuitive sense as a ‘‘cylindrical approximation’’.

B. Algorithms

We enumerate here the computational procedures used to approximate probabilities in Section VI and Section IX.

Algorithm 1 Monte Carlo Simulation - H1

Input: Path function $\mu_R(\mathbf{s})$ \triangleright Domain: $[0, 1]$
 Obstacle mean position μ_O
 Combined Covariance Σ_T
 Combined Radius r
 Number of Monte Carlo Trials N_t
 Discretization of the Path N_s
Output: Probability estimate \mathbf{P}_T
 Initialize collision counter $\mathbf{c} = \mathbf{0}$
for $j = 1$ to N_t **do** \triangleright Done in parallel
 for $s_i = 0$ to N_s **do**
 Sample μ_O^{*ij} from $\mathcal{N}(\mu_O, \Sigma_T)$
 Compute $d_i^j = \mu_R(\frac{s_i}{N_s}) - \mu_O^{*ij}$
 if $\text{norm}(d_i^j) \leq r$ **then**
 $c = c + 1$
 break for
 $\hat{\mathbf{P}} = \frac{\mathbf{c}}{N_t}$

Algorithm 2 Monte Carlo Simulation - H2

Input: $\mu_R(\mathbf{s}), \mu_O, \Sigma_T, r, N_t, N_s$
Output: Probability estimate \mathbf{P}_T
 Initialize collision counter $\mathbf{c} = \mathbf{0}$
for $j = 1$ to N_t **do** \triangleright Done in parallel
 for $s_i = 0$ to N_s **do**
 Sample μ_O^{*ij} from $\mathcal{N}(\mu_O, \Sigma_T)$
 if $s_i > 0$ **then** \triangleright Naïve Rejection Sampling
 Compute $dp_i^j = \mu_R(\frac{s_i-1}{N_s}) - \mu_O^{*ij}$
 while $\text{norm}(dp_i^j) \leq r$ **do**
 Sample μ_O^{*ij} from $\mathcal{N}(\mu_O, \Sigma_T)$
 Compute $dp_i^j = \mu_R(\frac{s_i-1}{N_s}) - \mu_O^{*ij}$
 Compute $d_i^j = \mu_R(\frac{s_i}{N_s}) - \mu_O^{*ij}$
 if $\text{norm}(d_i^j) \leq r$ **then**
 $c = c + 1$
 break for
 $\hat{\mathbf{P}} = \frac{\mathbf{c}}{N_t}$

Algorithm 3 Monte Carlo Simulation - H3

Input: $\mu_R(\mathbf{s}), \mu_O, \Sigma_T, r, N_t, N_s$
Output: Probability estimate \mathbf{P}_T
 Initialize collision counter $\mathbf{c} = \mathbf{0}$
for $j = 1$ to N_t **do** \triangleright Done in parallel
 Sample μ_O^{*j} from $\mathcal{N}(\mu_O, \Sigma_T)$
 for $s_i = 0$ to N_s **do**
 Compute $d_i^j = \mu_R(\frac{s_i}{N_s}) - \mu_O^{*j}$
 if $\text{norm}(d_i^j) \leq r$ **then**
 $c = c + 1$
 break for
 $\hat{\mathbf{P}} = \frac{\mathbf{c}}{N_t}$

Algorithm 4 Probability Estimate with Risk Density, Single Obstacle

Input: $\mu_R(\mathbf{s}), \mu_O, \Sigma_T, r$
Output: Probability estimate \mathbf{P}_a
 Compute rd eq. (42) with inputs $\mu_R(s), \mu_O, \Sigma_T$
 $\mathbf{P}_a = rd \cdot r$

Algorithm 5 Probability Estimate with Risk Density, Multiple Obstacles

Input: $\mu_R(\mathbf{s}), \bar{\mu}_O, \bar{\Sigma}_T, \bar{r}$ \triangleright Barred variables are vectors of their respective elements.
Output: Probability Estimate \mathbf{P}_a
 $\bar{rd} = \text{eq. (48) with inputs } \mu_R(s), \bar{\mu}_O, \bar{\Sigma}_T$
 $\mathbf{P}_a = \mathbf{rd}_0^T \cdot \bar{r}$

⁸Here $\Gamma(\gamma, T, \theta) = |f(\gamma, T, \theta)|$. The derivative $\frac{d\Gamma}{dT} = \frac{f}{T}(|\frac{d\mu_R}{d\gamma}| + T\kappa(\gamma) \cos(\theta))$ simplifies to $|\frac{d\mu_R}{d\gamma}|$ since $\lim_{T \rightarrow 0} \frac{f}{T} = 1$, being $T > 0$ by definition, cancelling out the fraction.

REFERENCES

- [1] T. Fraichard, "A Short Paper about Motion Safety," in *Proceedings 2007 IEEE International Conference on Robotics and Automation*. Rome, Italy: IEEE, Apr. 2007, pp. 1140–1145.
- [2] X. Xiao, J. Dufek, and R. R. Murphy, "Robot Risk-Awareness by Formal Risk Reasoning and Planning," *IEEE Robot. Autom. Lett.*, vol. 5, no. 2, pp. 2856–2863, Apr. 2020.
- [3] Masahiro Ono and B. C. Williams, "Iterative Risk Allocation: A new approach to robust Model Predictive Control with a joint chance constraint," in *2008 47th IEEE Conference on Decision and Control*. Cancun, Mexico: IEEE, 2008, pp. 3427–3432.
- [4] W. Han, A. Jasour, and B. Williams, "Non-Gaussian Risk Bounded Trajectory Optimization for Stochastic Nonlinear Systems in Uncertain Environments," Mar. 2022.
- [5] L. Blackmore, M. Ono, A. Bektassov, and B. C. Williams, "A Probabilistic Particle-Control Approximation of Chance-Constrained Stochastic Predictive Control," *IEEE Trans. Robot.*, vol. 26, no. 3, pp. 502–517, June 2010.
- [6] A. Lambert, D. Gruyer, and G. Saint Pierre, "A fast Monte Carlo algorithm for collision probability estimation," in *2008 10th International Conference on Control, Automation, Robotics and Vision*. Hanoi, Vietnam: IEEE, Dec. 2008, pp. 406–411.
- [7] A. B. Owen, *Monte Carlo Theory, Methods and Examples*, 2013.
- [8] K. Frey, T. Steiner, and J. How, "Collision Probabilities for Continuous-Time Systems Without Sampling," in *Robotics: Science and Systems XVI*. Robotics: Science and Systems Foundation, July 2020.
- [9] L. Janson, E. Schmerling, and M. Pavone, "Monte Carlo Motion Planning for Robot Trajectory Optimization Under Uncertainty," May 2015.
- [10] N. E. Du Toit and J. W. Burdick, "Probabilistic Collision Checking With Chance Constraints," *IEEE Trans. Robot.*, vol. 27, no. 4, pp. 809–815, Aug. 2011.
- [11] L. Blackmore and M. Ono, "Convex Chance Constrained Predictive Control Without Sampling," in *AIAA Guidance, Navigation, and Control Conference*. Chicago, Illinois: American Institute of Aeronautics and Astronautics, Aug. 2009.
- [12] A. Shapiro, D. Dentcheva, and A. Ruszczyński, *Lectures on Stochastic Programming: Modeling and Theory*. Society for Industrial and Applied Mathematics, Jan. 2009.
- [13] D. H. van Hessem, "Stochastic inequality constrained closed-loop model predictive control: With application to chemical process operation," 2004.
- [14] L. Blackmore, Hui Li, and B. Williams, "A probabilistic approach to optimal robust path planning with obstacles," in *2006 American Control Conference*. Minneapolis, MN, USA: IEEE, 2006, p. 7 pp.
- [15] J. S. Park, C. Park, and D. Manocha, "Efficient Probabilistic Collision Detection for Non-Convex Shapes," Oct. 2016.
- [16] C. Park, J. S. Park, and D. Manocha, "Fast and Bounded Probabilistic Collision Detection for High-DOF Trajectory Planning in Dynamic Environments," *IEEE Trans. Automat. Sci. Eng.*, vol. 15, no. 3, pp. 980–991, July 2018.
- [17] —, "Fast and Bounded Probabilistic Collision Detection for High-DOF Robots in Dynamic Environments," in *Algorithmic Foundations of Robotics XII*, K. Goldberg, P. Abbeel, K. Bekris, and L. Miller, Eds. Cham: Springer International Publishing, 2020, vol. 13, pp. 592–607.
- [18] L. Blackmore, M. Ono, and B. C. Williams, "Chance-Constrained Optimal Path Planning With Obstacles," *IEEE Trans. Robot.*, vol. 27, no. 6, pp. 1080–1094, Dec. 2011.
- [19] A.-a. Agha-mohammadi, "SMAP: Simultaneous Mapping and Planning on Occupancy Grids," Sept. 2016.
- [20] A. Elfes, "Using occupancy grids for mobile robot perception and navigation," *Computer*, vol. 22, no. 6, pp. 46–57, June 1989.
- [21] J. Laconte, C. Debain, R. Chapuis, F. Pomerleau, and R. Aufrere, "Lambda-Field: A Continuous Counterpart of the Bayesian Occupancy Grid for Risk Assessment," in *2019 IEEE/RSJ International Conference on Intelligent Robots and Systems (IROS)*. Macau, China: IEEE, Nov. 2019, pp. 167–172.
- [22] J. Lasserre, "The Moment-SOS hierarchy," Aug. 2018.
- [23] S. M. LaValle, *Planning Algorithms*. Cambridge: Cambridge University Press, 2006.
- [24] E. Gilbert, D. Johnson, and S. Keerthi, "A fast procedure for computing the distance between complex objects in three-dimensional space," *IEEE J. Robot. Automat.*, vol. 4, no. 2, pp. 193–203, Apr. 1988.
- [25] H. Pishro-Nik, *Probability, Statistics & Random Processes*, 2014.
- [26] J. L. Speyer and W. H. Chung, *Stochastic Processes, Estimation, and Control*, 1st ed., ser. Advances in Design and Control. Philadelphia: Society for Industrial and Applied Mathematics, 2008, no. 17.
- [27] J. van den Berg, P. Abbeel, and K. Goldberg, "LQG-MP: Optimized path planning for robots with motion uncertainty and imperfect state information," *The International Journal of Robotics Research*, vol. 30, no. 7, pp. 895–913, June 2011.
- [28] S. Patil, J. van den Berg, and R. Alterovitz, "Estimating probability of collision for safe motion planning under Gaussian motion and sensing uncertainty," in *2012 IEEE International Conference on Robotics and Automation*. St Paul, MN, USA: IEEE, May 2012, pp. 3238–3244.
- [29] R. G. Gallager, *Stochastic Processes: Theory for Applications*. Cambridge, United Kingdom ; New York: Cambridge University Press, 2013.
- [30] Y. de Mont-Marin, J. Ponce, and J.-P. Laumond, "A minimum swept-volume metric structure for configuration space," 2022. [Online]. Available: <https://arxiv.org/abs/2211.11811>
- [31] L. Paiola, G. Grioli, and A. Bicchi, "Considerations on possible approaches to measure risk for obstacle avoidance," in *Fourth Italian Conference on Robotics and Intelligent Machines (I-RIM)*. Rome, Italy: Zenodo, Oct. 2022.
- [32] A. Slavík, *Product Integration, Its History and Applications*, ser. History of Mathematics. Praha: Matfyzpress, 2007, no. 29.
- [33] N. E. Du Toit and J. W. Burdick, "Robot Motion Planning in Dynamic, Uncertain Environments," *IEEE Trans. Robot.*, vol. 28, no. 1, pp. 101–115, Feb. 2012.
- [34] J. Nocedal and S. J. Wright, *Numerical Optimization*, second edition ed., ser. Springer Series in Operation Research and Financial Engineering. New York, NY: Springer, 2006.